

1        **Baseflow in karst regions is significantly higher than the**  
2                    **global average and exhibits spatial variability**

3  
4 Author :Ze Yuan <sup>a,b</sup>, Qiuwen Zhou <sup>a,b\*</sup>, Yuan Li <sup>a,b\*</sup>, Yuluan Zhao <sup>a,b</sup>, Shen  
5 gtian Yang <sup>c,d</sup>

6 Affiliation:

7 a. School of Geography and Environmental Science, Guizhou Normal Un  
8 iversity, 550001 Guiyang, China

9 b. Karst Ecosystem Field Scientific Observation and Research Station of  
10 Guizhou Normal University & Guanling Autonomous County, 561300 G  
11 uanling, China

12 c. Institute of Ecological Civilization, Guizhou Normal University, 55000  
13 1 Guiyang, China

14 d. College of Water Sciences, Beijing Normal University, 100875 Beijing,  
15 China

16 Corresponding author: Qiuwen Zhou \*, Yuan Li\*

17 Email: zqw@gznu.edu.cn, Yuan Li: liyuan7pro@163.com

18

19

20 Abstract: The distinct hydrogeological configurations of karst terrains engender  
21 fundamentally divergent baseflow regimes compared with non-karst systems. However,  
22 there is still some uncertainty in the understanding of baseflow in global karst regions  
23 due to the variability of methods and differences in natural conditions in different  
24 regions. In this study, runoff data from 1375 karst basins around the world were  
25 summarized. Graphical and digital filtering methods were employed to estimate the  
26 Baseflow Index (BFI, defined as the ratio of baseflow to total streamflow) and to  
27 analyze its spatial patterns and trends. The results show that the baseflow index of  
28 global karst areas is about  $78 \pm 6.9\%$ , which is significantly higher than the global  
29 average baseflow index (60%). The baseflow index of karst regions in different climatic  
30 zones also differed significantly, in which the average baseflow index of arid karst  
31 regions (82%) was significantly higher than the average baseflow index of subtropical  
32 karst regions (77%). Even within the same climate zone, the base flow index of different  
33 regions may also have significant differences, and the difference of some regions is  
34 even  $>10\%$ . Vegetation factors reflected in primary productivity have the highest  
35 influence on baseflow in karst regions (14.8%), while climatic factors (relative humidity,  
36 air temperature, etc.) have a lower influence on BFIs in karst regions (less than 5%).  
37 From the time series trend, the global karst baseflow index shows an increasing trend,  
38 about 1.5% from 1960 to 2015. These results help us to further understand karst  
39 hydrological processes and the response mechanism of karst hydrology under climate  
40 change.

41

42 Key words: Baseflow; Karst; Hydrographic graphical method; climate zone; global  
43 runoff data; hydrogeology

44

## 1. Introduction

Functioning as a vital component of groundwater recharge to runoff, baseflow acts as a critical hydrological stabiliser (Mukherjee et al., 2018; Chen et al., 2019). The proportion and dynamic characteristics of baseflow in runoff (commonly quantified as the Baseflow Index, BFI) not only regulate the ecological balance threshold of rivers, but also profoundly affect the resilience of watersheds in response to climate fluctuations (Saedi et al., 2022; Hare et al., 2021; Yang et al., 2023). Therefore, accurate quantification of the characteristics of baseflow can help to understand the runoff evolution pattern and its response mechanism to regional environmental changes (Mei et al., 2024; Kuehne et al., 2023).

Recent studies on baseflow estimation have revealed its spatial variability characteristics. Among them, Xie et al (2023), based on a coupled analysis of baseflow separation and climate models for 15,000 catchments worldwide, pointed out that the average contribution of baseflow to river runoff was about 60%. However, there are significant regional differences under this macroscopic pattern, e.g., baseflow index (BFI) calculations by Beck et al (2013) for 3,394 watersheds globally show that BFI is generally higher in tropical and temperate-cold regions than in arid and semi-arid zones (e.g., North and South Africa, Central Asia, and Australia). Regional-scale studies further refine these spatial patterns. For instance, the BFI is observed to be higher in the eastern regions of both the United States and India compared to their western counterparts (Mei et al., 2024; Sharma and Mujumdar, 2024). In China, the Yellow River Basin exhibits a 'high-low-high' trend from upstream to downstream, whereas the Wei River Basin shows a gradual decline (Lyu et al., 2023; Zhang et al., 2019).

While current research characterizes general global baseflow features, the distinct hydrogeological architecture of karst landscapes (e.g., conduit and fissure networks) renders these findings significantly less applicable to karst regions (Jing et al., 2024; Ford & Williams, 2007). Observations indicate significant heterogeneity in karst BFI across different climatic zones, which are typically categorized by hydrothermal conditions (e.g., the Köppen classification). In Tropical zones (characterized by high temperature and humidity), the high permeability of karst media facilitates rapid precipitation-to-groundwater conversion; for instance, sub-basins in the Brantas Hulu watershed (Pratama and Adji, 2020) exhibit BFIs exceeding 80%. Conversely, Arid and Semi-arid regions (defined by water limitation) often show distinct recharge patterns due to scarcity of rainfall. In Subtropical zones, where seasonality is moderate but

79 distinct, baseflow contributions can vary drastically; in central Italy, BFI ranges from  
80 30 - 76% annually (Longobardi and Loon, 2017). Similarly, Temperate zones display  
81 diverse patterns, such as the Sierra Nevada karst in North America maintaining a BFI  
82 above 65% (Tobin and Schwartz, 2019). These disparities highlight the need to consider  
83 climatic classification when analyzing global karst hydrology.

84 In summary, studies of baseflow in karst regions have revealed their obvious  
85 spatial heterogeneity. A large number of studies have characterised the baseflow  
86 characteristics of karst under different climatic zones, and also outlined the regional  
87 baseflow characteristics of karst under different climatic zones (Tagne and Dowling.,  
88 2018). However, existing studies still have obvious limitations, starting with an over-  
89 focus on localised features in small regions, such as watershed studies in southern China  
90 and the Mediterranean (Guisiano et al., 2024; Mo and Ruan., 2021), which makes the  
91 results of the study not necessarily representative of the global karst region. The second  
92 is the variability of research methods, such as hydrographic methods (graphical  
93 methods, digital filtering methods), isotope tracer methods, etc. (He et al., 2019; Yang  
94 et al., 2021; Arnold et al.,2013). The difference in focus of the different methods also  
95 reduces the commonality of the findings. These two reasons have led to a lack of  
96 characterisation of overall features and reasonable quantification of regional differences,  
97 despite the exploration of baseflow characteristics of karst basins in different regions  
98 of the world (Wu et al., 2017; Mei et al., 2024). Therefore, the complete characterisation  
99 of baseflow in the global karst region using reasonable methods and the accurate  
100 quantification of the overall characteristics and regional differences of baseflow in the  
101 global karst region are still urgently needed.

102 The overarching aim of this study is to explore the baseflow characteristics and  
103 their internal differences across global karst regions, and to evaluate the influence of  
104 different environmental factors on these characteristics. To achieve this, the following  
105 four specific objectives are defined:(i) To evaluate the applicability of twelve baseflow  
106 separation methods (including graphical and digital filter methods) in karst watersheds  
107 and identify the most suitable approaches.(ii) To reveal the unique hydrological  
108 signature of karst baseflow and analyze its spatiotemporal evolution characteristics  
109 under changing climate conditions.(iii) To quantify the heterogeneity of baseflow  
110 across different karst landform types and clarify the internal differences.(iv) To identify  
111 the dominant climatic, topographic, and geological drivers of baseflow variability using  
112 an XGBoost machine learning model.

## 113 2. Materials and methods

### 114 2.1 Data sources

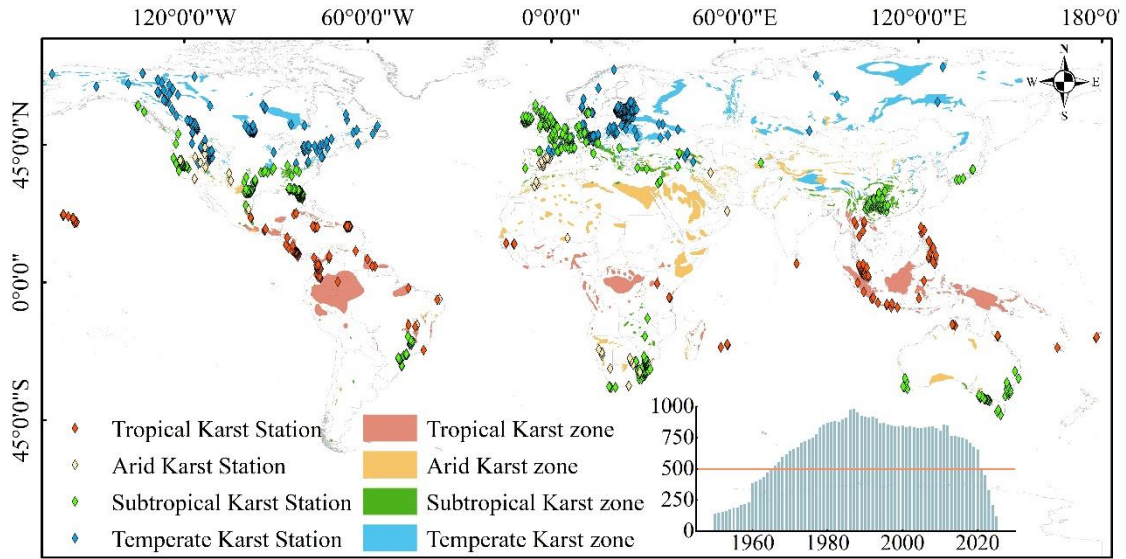
#### 115 2.1.1 Runoff data

116 This study focuses on regions with extensive karst landscape distribution globally.  
117 By overlaying global watershed boundaries (Lehner and Grill, 2013), Köppen climate  
118 zones, and urban distribution maps, we identified candidate runoff observation stations.  
119 To minimize anthropogenic disturbance, only watersheds with limited human activity  
120 and areas smaller than 2,500 km<sup>2</sup> were selected. Thus daily runoff data for 1412  
121 watersheds with different time spans have been selected. The runoff data mainly comes  
122 from the Global Runoff Data Center (<https://www.bafg.de/GRDC>), The European  
123 Water Archive (<https://ne-friend.bafg.de/servlet/>), National River Flow Archive, UK  
124 (<https://nrfaapps.ceh.ac.uk/nrfa/nrfa-api.html>), Brazilian National Water Authority  
125 (<https://zenodo.org> ), The National Hydrological Data Archive of Canada  
126 (<https://wateroffice.ec.gc.ca/>), The Chinese Ministry of Water Resources  
127 (<http://www.cjh.com.cn/>), The National Hydrological Information System of the United  
128 States (<https://waterdata.usgs.gov/nwis>).

129 Initially, data from 1,412 hydrological stations were compiled. To ensure data  
130 quality, a rigorous screening process was applied. Stations with severe data gaps or  
131 extensive periods of zero flow were excluded. For stations with minor gaps (less than  
132 30 days), missing values were filled using cubic spline and linear interpolation. This  
133 process resulted in a final dataset of 1,375 valid karst watersheds covering the period  
134 from 1960 to 2015. These watersheds are distributed across different climatic zones,  
135 including 221 in tropical, 91 in arid, 490 in subtropical, and 568 in temperate karst  
136 regions (Figure 1).

137 To ensure consistent climatic characterization, we adopted the Köppen-Geiger  
138 climate classification system (Peel et al., 2007) to categorize these watersheds.  
139 Specifically, "Tropical karst" corresponds to the equatorial zone (Group A),  
140 characterized by high temperatures and precipitation year-round. "Arid karst" falls  
141 under the arid zone (Group B), defined by water scarcity. "Subtropical karst" primarily  
142 includes the warm temperate climates (Group C, e.g., Cfa, Cwa) with hot summers,

143 while "Temperate karst" encompasses the snow climates (Group D) and cool temperate  
 144 regions (e.g., Cfb), featuring distinct seasonal contrasts and colder winters.



145  
 146 Figure 1. The distribution of karst landscapes and hydrological stations in various  
 147 climate zones around the world. The bar chart represents the number of hydrological  
 148 stations selected in each year, with the vertical axis indicating the number of selected  
 149 hydrological stations and the horizontal axis indicating the year. We selected years with  
 150 over 500 hydrological stations that meet the requirements within the same year for  
 151 subsequent analysis.

### 152 2.1.2 Selection of potential influencing factors of baseflow

153 In order to analyse the influencing factors of baseflow, we further selected daily-  
 154 scale runoff data from 744 hydrological stations during 2011-2012 out of the 1375  
 155 hydrological stations mentioned earlier to calculate baseflow. The purpose of further  
 156 selecting the hydrological stations is to ensure the continuity of the data while at the  
 157 same time ensuring that the stations can cover the major karst regions of the world. We  
 158 selected a total of 12 potential influences. Climatic factors included temperature and  
 159 rainfall, and geological factors included depth to bedrock, water storage in epikarst,  
 160 slope, elevation, and soil evaporation. Other factors included runoff, population density,  
 161 gross primary productivity (GPP), relative humidity, and surface radiation, for a total  
 162 of 12 factors (Table 1).

163 Table 1. Detailed information on the 12 influencing factors

Name	Temporal scale	Spatial resolution	Data sources
Runoff volume	Monthly average	-	The same as the runoff data in Section 2.1.1
Epikarst water	Monthly	30 arc-second	GES (Goddard Earth Sciences) DISC (Li

storage volume	average		et al.,2019)
Bedrock depth	-	0.25km×0.25 km	ISRIC — World Soil Information (Hengl et al.,2017)
Air temperature	Monthly average	30 arc-second	
Precipitation	Monthly average	30 arc-second	Climatic Research Unit gridded Time Series (arris et al.,2020)
Relative humidity	Monthly average	0.1°×0.1°	
Elevation	-	30 arc-second	Worldclim (Fick and Hijmans.,2017)
Slope steepness	-	30 arc-second	
Available soil moisture	multi-year average	1km×1km	HWSD (Harmonized World Soil Database) (Wieder et al.,2014)
Population density	multi-year average	30 arc-second	LandScan Global 30 Arcsecond Annual Global Gridded Population Datasets (Bright et al., 2013)
Gross primary production	multi-year average	0.25°×0.25°	TU Data Repository (Wild et al.,2022)
Land-surface radiation	Monthly average	10km	Data Center of the Qinghai-Tibet Plateau (Tang.,2019)

164

## 165 2.2 Methods

### 166 2.2.1 Baseflow separation methods

167 Commonly used methods for baseflow separation include isotope tracer methods,  
168 hydrological modeling, and hydrograph analysis (graphical methods and digital  
169 filtering). Isotope methods require high-precision data often unavailable in data-scarce  
170 regions, while hydrological models are frequently limited by parameter uncertainty and  
171 regional applicability.

172 Given the global scale and data constraints of this study, we selected hydrograph  
173 analysis methods for their data efficiency and robustness. We utilized the baseflow  
174 Python library developed by Xie et al. (2024) to implement the separation. This tool  
175 integrates 12 distinct methods, comprising four graphical methods and eight digital  
176 filtering methods. Table 2 provides a detailed summary of the principles and references  
177 for each method. For the digital filtering methods, parameter estimation is critical. The  
178 recession constant(  $\alpha$  ) was automatically estimated using the Brutsaert (2008) method.  
179 Secondary parameters, where applicable, were calibrated using the multi-objective  
180 optimization approach proposed by Arnold (Rammal et al., 2018). The baseflow library

181 automatically evaluates the performance of these methods to determine the optimal  
 182 separation for each watershed.

183 Since different methods rely on different assumptions, their performance varies  
 184 across watersheds. To address this, we employed an optimization strategy provided by  
 185 the baseflow library. The performance of each method was evaluated by comparing the  
 186 separated baseflow with the observed streamflow during recession periods (when  
 187 streamflow is assumed to be purely baseflow). The evaluation metrics included the  
 188 Nash-Sutcliffe Efficiency (NSE) and Kling-Gupta Efficiency (KGE). For each of the  
 189 1,375 watersheds, the method yielding the highest evaluation scores was selected as the  
 190 optimal method for subsequent analysis. This approach minimizes the uncertainty  
 191 associated with selecting a single arbitrary method for global-scale analysis.

Table 2: Explanation of 12 Baseflow Separation Methods

Category	Method (Abbreviation)	Key Principle / Description
Graphical	Fixed Interval (FIM)	Segments hydrograph into fixed intervals; takes minimum flow in each interval as baseflow.
	Local Minimum (LMM)	Identifies local minimum points in the flow time series to demarcate baseflow.
	Sliding Window (SW)	Traverses hydrograph with a fixed-width window, assigning minimum flow to the center point.
	UK Institute of Hydrology (UKIH)	Identifies turning points based on precipitation thresholds and flow response logic.
Digital Filter	Boughton	Single-parameter recursive filter relating current baseflow to previous baseflow and total flow.
	Chapman- Maxwell (CM)	Enhances Chapman filter by dynamically adjusting the recession constant.
	Chapman	Weighted average of current total flow and previous baseflow; corrects constant baseflow issues.
	EWMA	Estimates baseflow by applying exponential weighting to smooth the streamflow series.
	Eckhardt	Two-parameter recursive filter evaluating maximum recession constant and maximum BFI.

Furey	Based on physical-statistical modeling of hillslope processes using recession constant.
Lyne-Hollick (LH)	Two-pass filtering process based on signal processing principles.
Willems	Based on a linear reservoir model and least squares optimization.

192

## 193 2.2.2 Evaluation metrics for baseflow separation methods

194 In order to validate the accuracy of different baseflow separation methods in karstic  
 195 regions, we chose two performance metrics: the KGE and NSE coefficients.  
 196 Theoretically, these coefficients vary from  $-\infty$  to 1; values closer to the maximum of 1  
 197 indicate higher accuracy, while values below 0 typically suggest unacceptable  
 198 performance. The assessment methodology followed Xie et al. (2020), centering on the  
 199 screening of strict baseflow points to benchmark the separation methods.

200 The core of screening strict baseflow points lies in excluding periods with  
 201 precipitation recharge and anomalies in the runoff curve, retaining only the stages where  
 202 baseflow acts as the primary runoff source. In such stages, there should be a distinct  
 203 consistency between baseflow and runoff. Therefore, using NSE and KGE coefficients  
 204 as evaluation criteria can reasonably assess the effectiveness of baseflow separation  
 205 methods.

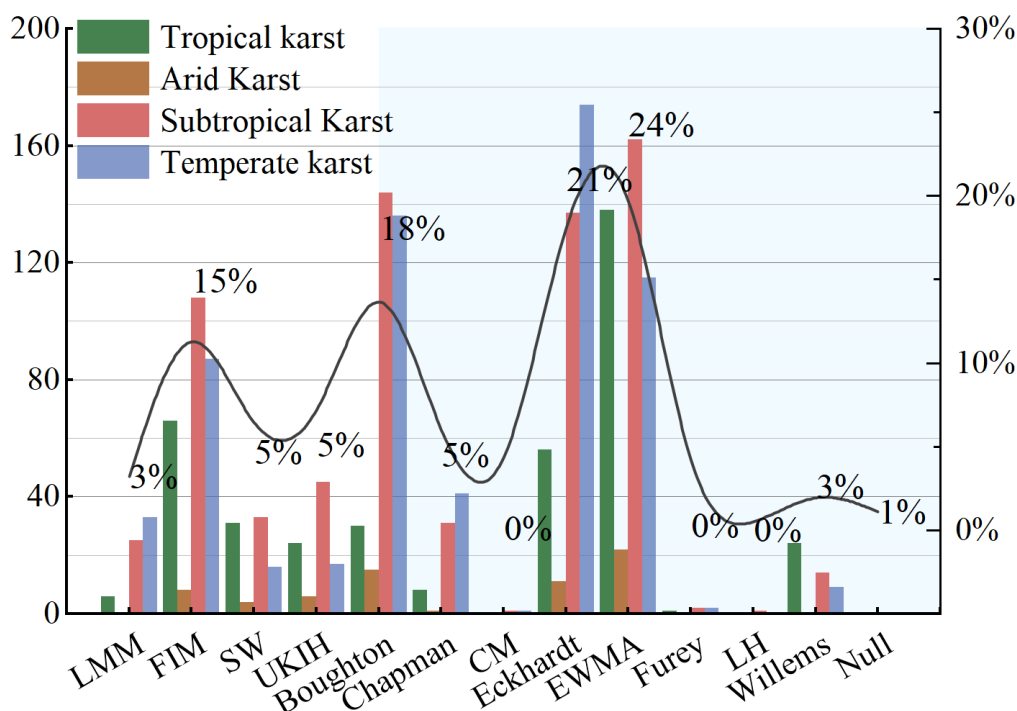
## 206 2.2.3 Attributional analysis methods

207 Due to the significant differences in magnitude of the potential influences selected  
 208 at the global scale (a few hydrological stations are at extremely high elevations, whose  
 209 actual differences are compressed after normalisation, making it difficult to adequately  
 210 characterise the effect of elevation on baseflow), traditional linear models or distance  
 211 metric-based algorithms are susceptible to magnitude interference. Therefore, we chose  
 212 the magnitude-insensitive XGBoost model, which naturally circumvents the feature  
 213 scale difference problem through the splitting rule of the tree structure (Niazkar et  
 214 al.,2024; Zhang et al., 2022). In addition, the model's built-in regularisation mechanism  
 215 and subsampling strategy can effectively suppress overfitting and guarantee the model's  
 216 generalisation ability in complex geographic data. The model also supports parallel  
 217 computing with automatic processing of missing values, which significantly improves  
 218 the computational efficiency of large-scale spatial datasets (Chen and Guestrin.,2016).

## 219 3. Results

### 220 3.1 Validation of the applicability of baseflow separation methods

221 Based on the screening results from the Baseflow library, we identified the optimal  
 222 baseflow separation method for each hydrological station. As shown in Figure 2, digital  
 223 filter methods proved most suitable for the majority of stations (71%), while graphical  
 224 methods were optimal for 28%. Only 1% of the stations showed no distinct preference  
 225 for any specific method. Specifically, the Exponential Weighted Moving Average  
 226 (EWMA) filter emerged as the most effective technique for karst regions, being the  
 227 optimal choice for 24% of the watersheds. This was followed closely by the Eckhardt  
 228 filter, which was suitable for 21% of the stations.



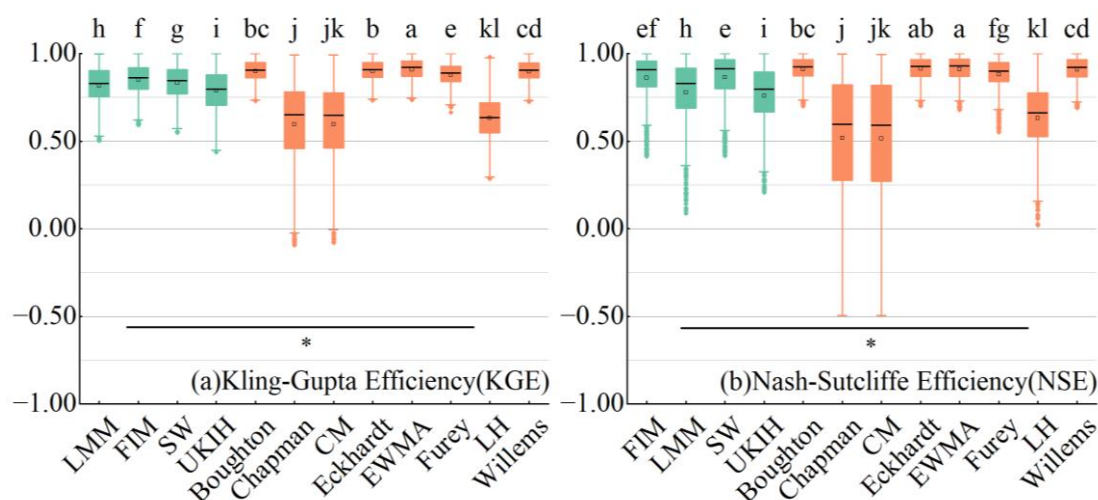
229  
 230 Figure 2. Percentage of best separation methods in the karst region and number of best  
 231 separation methods in each climatic zone. Graphical methods are shown within the  
 232 white background, digital filtering methods are shown within the light blue background,  
 233 and different coloured bars correspond to different climatic zones. The X-axis shows  
 234 the 12 baseflow separation methods, the Y-axis (left) shows the number of hydrological  
 235 stations, and the Y-axis (right) shows the number of hydrological stations covered by  
 236 each of the optimal baseflow separation methods as a proportion of the number of all  
 237 hydrological stations, which corresponds to the black curve.

238 **Figure 3(a) illustrates the KGE coefficient distributions for the different baseflow**  
 239 **separation methods. Among the digital filtering methods (orange), Boughton, Eckhardt,**  
 240 **EWMA, Furey, and Willems exhibit highly concentrated distributions with medians**  
 241 **approaching 1, indicating their strong applicability in the karst region. According to the**  
 242 **significance analysis (indicated by the letters above the boxplots), EWMA is identified**

243 as the optimal method (labeled 'a'). Meanwhile, Boughton ('bc'), Eckhardt ('b'), and  
 244 Willems ('cd') share overlapping significance groupings, suggesting no statistically  
 245 obvious disparity in their high performance.

246 In contrast, the Chapman, CM, and LH methods display highly dispersed  
 247 distributions with long whiskers extending into negative values, indicating significant  
 248 instability when processing data from different hydrological stations. Despite these  
 249 fluctuations, the overlapping significance letters ('j', 'jk', 'kl') confirm there is no  
 250 significant difference among these three lower-performing methods. For the graphical  
 251 methods (green), the KGE coefficients are well-distributed (mostly > 0.5), though their  
 252 letters ('f' through 'i') indicate they statistically rank below the top-tier digital filters.  
 253 Furthermore, the horizontal line with an asterisk (\*) at the bottom signifies a statistically  
 254 significant difference ( $p < 0.05$ ) between the graphical methods and the digital filtering  
 255 methods as distinct categories.

256 The distribution pattern of the NSE coefficients in Figure 3(b) mirrors that of  
 257 Figure 3(a). The EWMA method maintains its status as the optimal sequence (labeled  
 258 'a'), while Eckhardt ('ab'), Boughton ('bc'), and Willems ('cd') again form a cluster of  
 259 high-performing methods with comparable statistical results. The graphical methods  
 260 show stable distributions with means above 0.5, whereas the Chapman, CM, and LH  
 261 methods remain highly discrete with wide ranges (-0.5 to 1). Consistent with the KGE  
 262 results, the significance test in Figure 3(b) confirms a significant difference ( $p < 0.05$ )  
 263 between the overall performance of graphical methods and digital filtering methods.

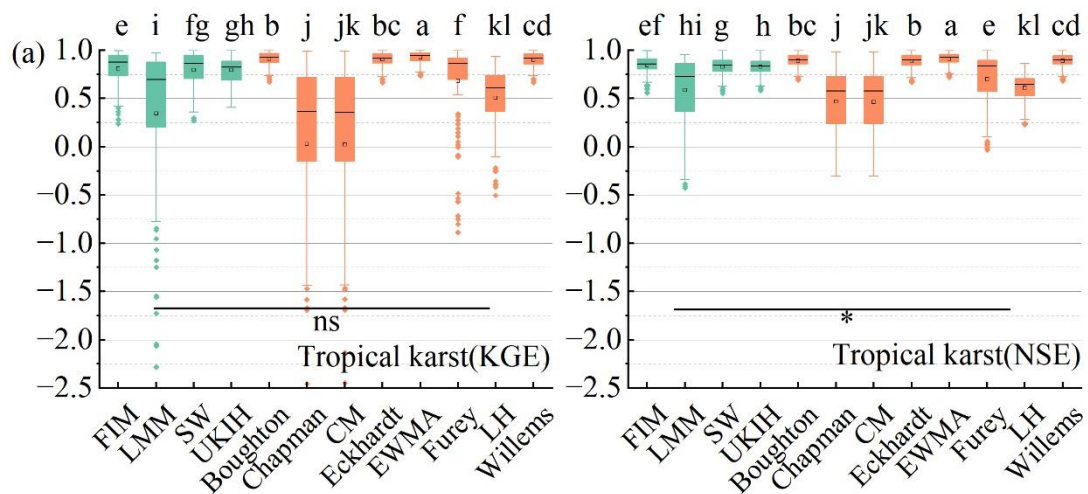


264  
 265 Figure 3. Comparison of KGE coefficients (a) and NSE coefficients (b) for the 12  
 266 baseflow separation methods. The X-axis represents each separation method, and the  
 267 Y-axis indicates the value of the coefficients. Green color in the plot denotes the  
 268 graphical method, while orange denotes the digital filtering method. The letters above

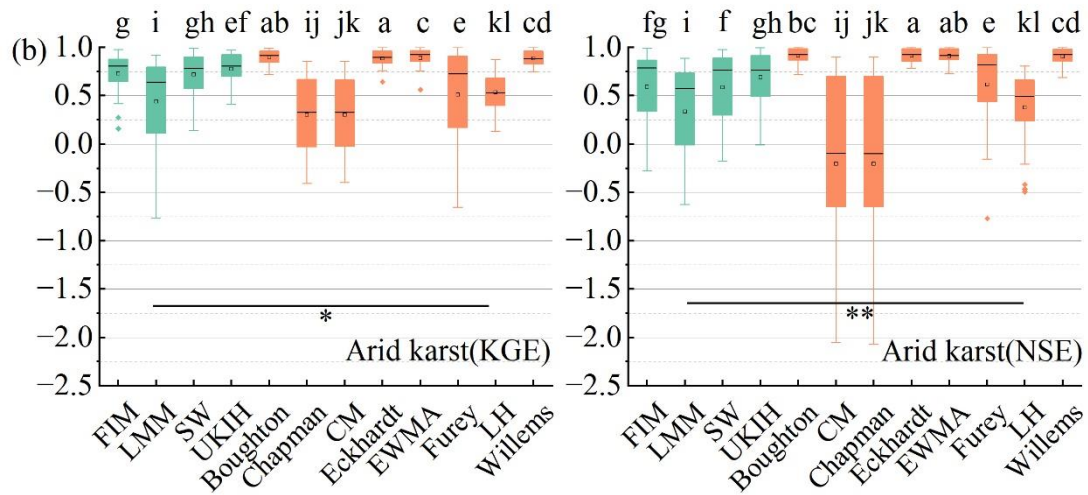
269 the boxes indicate significant differences among the different baseflow separation  
 270 methods, while the horizontal lines in the lower part of the figure represent significant  
 271 differences between the graphical method and the digital filtering method. The black  
 272 line inside the boxplot denotes the mean value, with upper and lower limits set at 1.5  
 273 times the interquartile range (IQR). Values exceeding this range are considered outliers  
 274 and are marked as dots at the top and bottom of the boxplot.

275 From the distribution characteristics of KGE and NSE coefficients in different  
 276 climatic zones (Figure 4), it is evident that the distribution patterns of these two  
 277 coefficients across different zones are generally consistent with the overall coefficient  
 278 characteristics. Specifically, the KGE coefficients of multiple separation methods in  
 279 tropical karst have discrete distributions, with CM and Chapman ranging from -1.5 to  
 280 1. The NSE coefficients are similar to those of the KGE, but with a relatively centralised  
 281 distribution. The distribution of coefficients of graphical methods in the arid karst  
 282 region are all discrete, and the The distribution of KGE coefficients in subtropical  
 283 and temperate karst is relatively stable and concentrated, and the overall distribution of  
 284 KGE coefficients of Chapman and CM are also discrete, while the KGE coefficients of  
 285 FIM and SW are close to 1, which indicates that these methods are more effective in  
 286 separating the baseflow in subtropical and temperate karst regions.

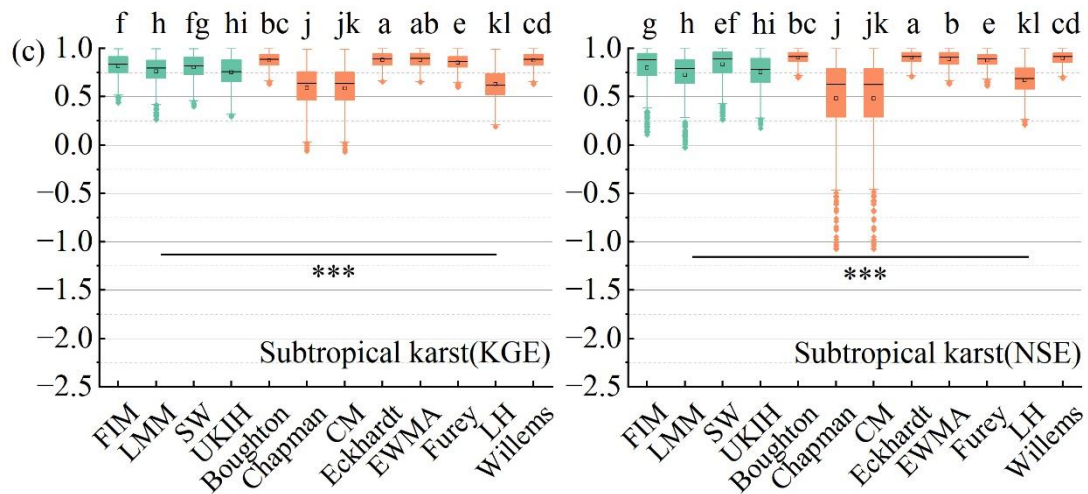
287 According to Figures 2 and 3, considering the high KGE and NSE coefficients and  
 288 the number of most suitable hydrological stations, we selected four more suitable  
 289 methods for baseflow separation in karst regions, which are one graphical method (FIM)  
 290 and three digital filtering methods (Boughton, Eckhardt, EWMA).



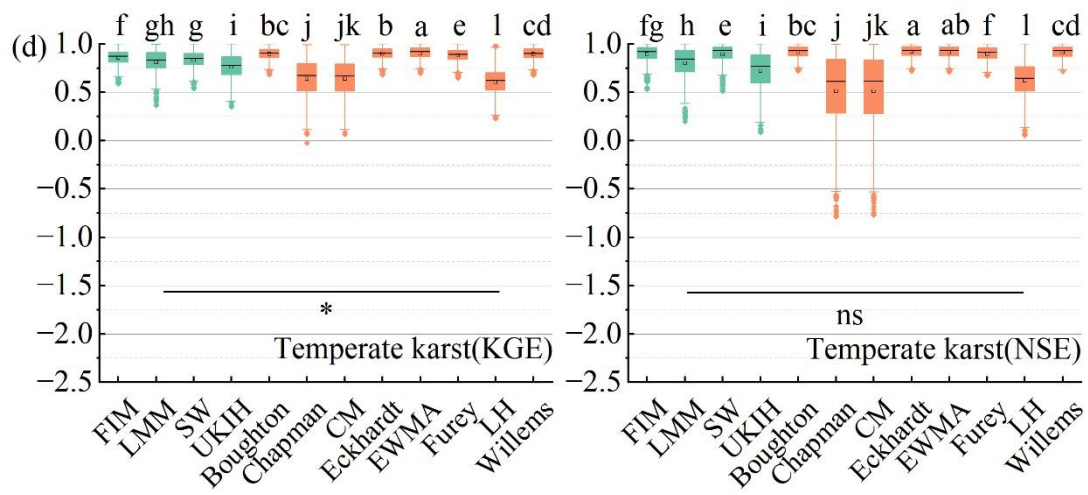
291



292



293



294

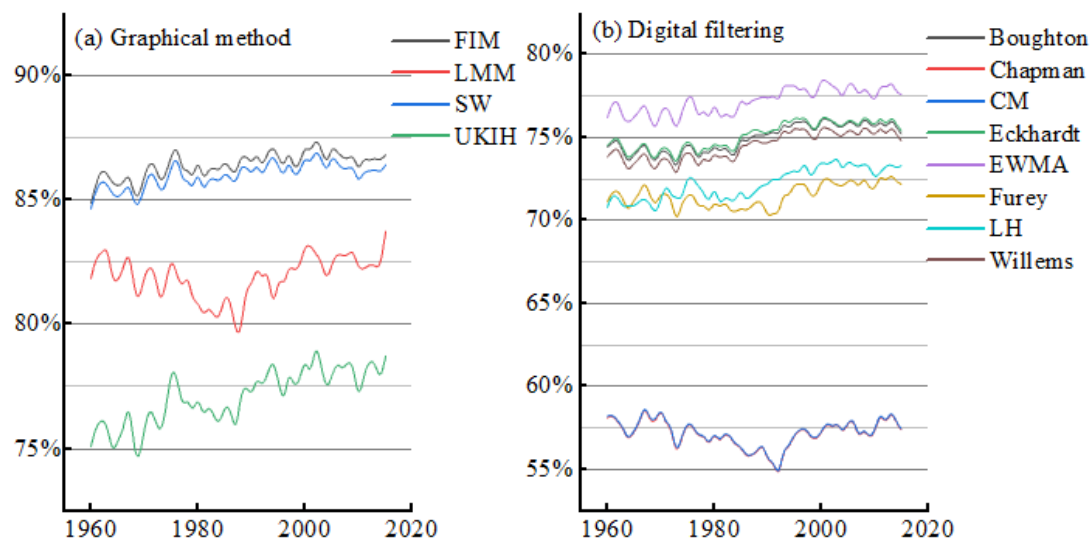
295 **Figure 4. Comparison of KGE coefficients (left) and NSE coefficients (right) for karst**  
 296 **regions in different climatic zones (as labeled in the bottom-right corner of each**  
 297 **subplot). The X-axis represents each separation method, and the Y-axis indicates the**  
 298 **coefficient values. The letters above the boxes indicate significant differences among**

299 the baseflow separation methods, while the horizontal lines in the lower part of the  
 300 figure denote significant differences between the graphical and digital filtering method  
 301 groups. Green color in the plot denotes the graphical method, and orange represents the  
 302 digital filtering method. The black line inside each boxplot indicates the mean value,  
 303 with the upper and lower limits set at 1.5 times the interquartile range (IQR). Data  
 304 points beyond this range are considered outliers and are marked as dots at the top and  
 305 bottom of the boxplot.

### 306 3.2 Differences in baseflow indices obtained by different methods 307 over time

308 From Figure 5a, it can be found that the four graphical methods have different  
 309 effects on baseflow separation in karst regions. Among them, the BFIs derived by FIM  
 310 and SW are similar, with an average value of about 86%. Moreover, the BFI shows an  
 311 increasing trend of low amplitude with the year, with low fluctuation degree and high  
 312 stability. The mean value of BFI derived from LMM is about 83%, and the trend of  
 313 change with years shows a decreasing and then increasing trend, while the result of  
 314 UKIH method is low, with a mean value of about 77%, and its BFI also shows a slow  
 315 increasing trend with years.

316 The results in Figure 5b can be found that although there are differences in the base  
 317 flow indices obtained by different digital filtering methods, most of the methods obtain  
 318 similar base flow indices and have similar trends with respect to year. In contrast, the  
 319 results of the two methods Chapman and CM differ significantly from those of the other  
 320 six methods. The mean value of the BFI obtained by the two methods is about 58%,  
 321 and there is a small decrease followed by a slow increase in the trend.

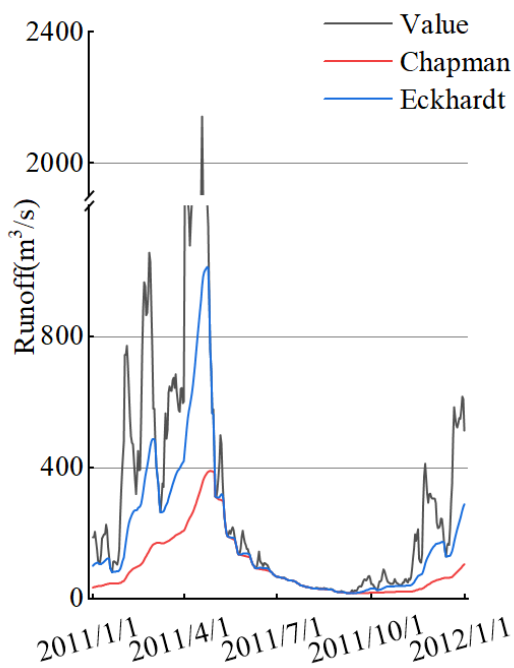


322  
 323 Figure 5. Global BFIs for karst regions calculated by the 12 baseflow separation

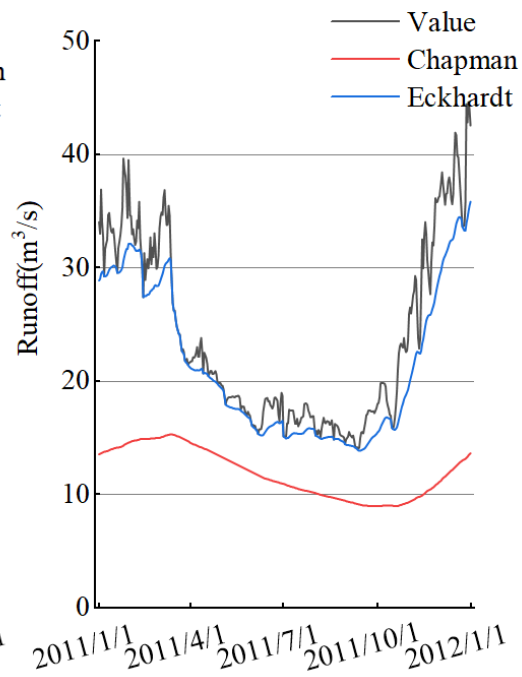
324 methods, with the x-axis indicating the year and the y-axis the BFI.

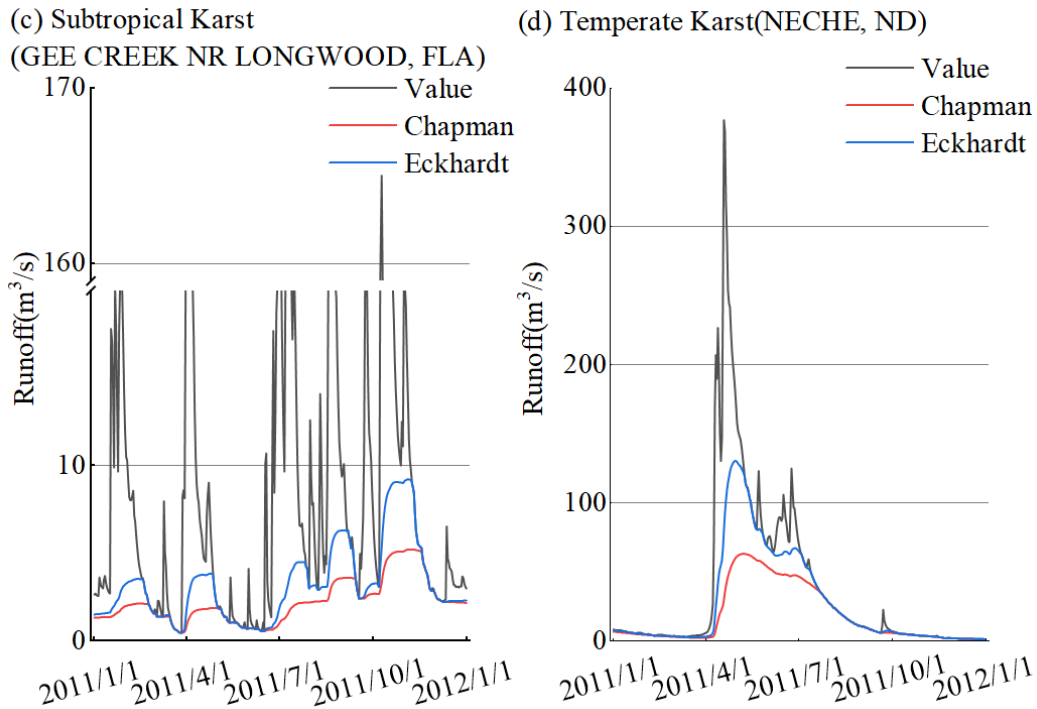
325 In order to analyze the reasons for the differences between these two methods (CM  
326 and Chapman) and other methods in separating baseflows, we selected one hydrological  
327 station in each climatic zone and generated baseflow curves obtained by the different  
328 methods in different climatic zones (Figure 6). Since the CM method is an improvement  
329 of Chapman by adding a maximum baseflow limit to the Chapman method, and its  
330 internal mechanism is consistent, Chapman was used as a proxy. In addition, the  
331 Eckhardt method with high KGE and NSE coefficients is chosen as a comparison. From  
332 Figure 6, we find that when runoff increases, the Eckhardt method can respond quickly  
333 and baseflow increases rapidly, while the Chapman method responds to the increase in  
334 runoff to a lesser extent and by a lower amount than Eckhardt. Overall, Chapman  
335 responds more slowly to the recharge of precipitation than the other methods, and this  
336 feature also makes the Chapman method less discriminating for baseflow compared to  
337 the other methods.

(a) Tropical Karst(RIO BRANCO)



(b) Arid Karst(LA ANGOSTURA)





339

340

341

342

343

Figure 6. baseflow curves for different climatic zones (Eckhardt and Chapman methods were chosen as representatives), where the X-axis represents time and the Y-axis represents runoff. The black curve (Value) represents the runoff volume. Names of hydrological stations are in parentheses.

344

### 3.3 Global base flow characteristics

345

346

347

348

349

350

In order to more clearly characterize the BFI in karst basins, we calculated the BFI in non-karst basins globally using the same method. Figure 7 shows that BFIs in karst basins are significantly higher than in non-karst basins. The BFI of karst basins is  $78 \pm 6.9\%$ , while the BFI of non-karst basins is about 60%. This indicates that baseflow in karst basins is significantly underestimated if only global average conditions are considered and baseflow in karst basins is not calculated separately.

351

352

353

354

355

356

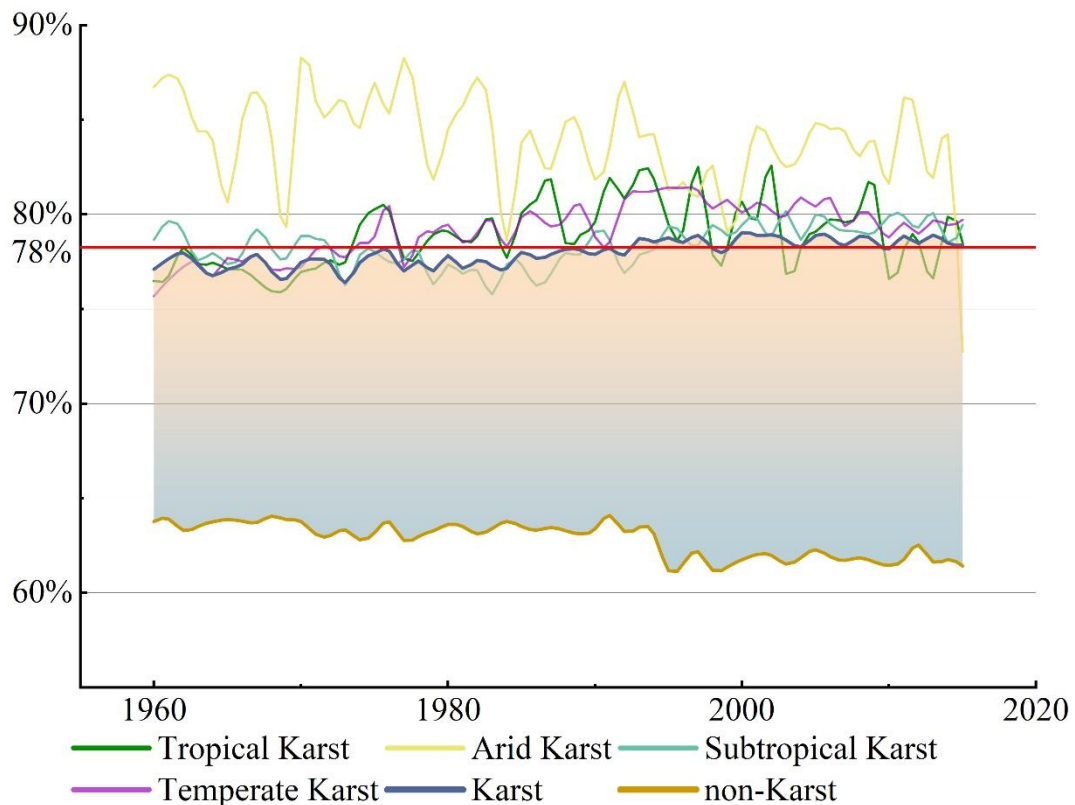
357

358

359

360

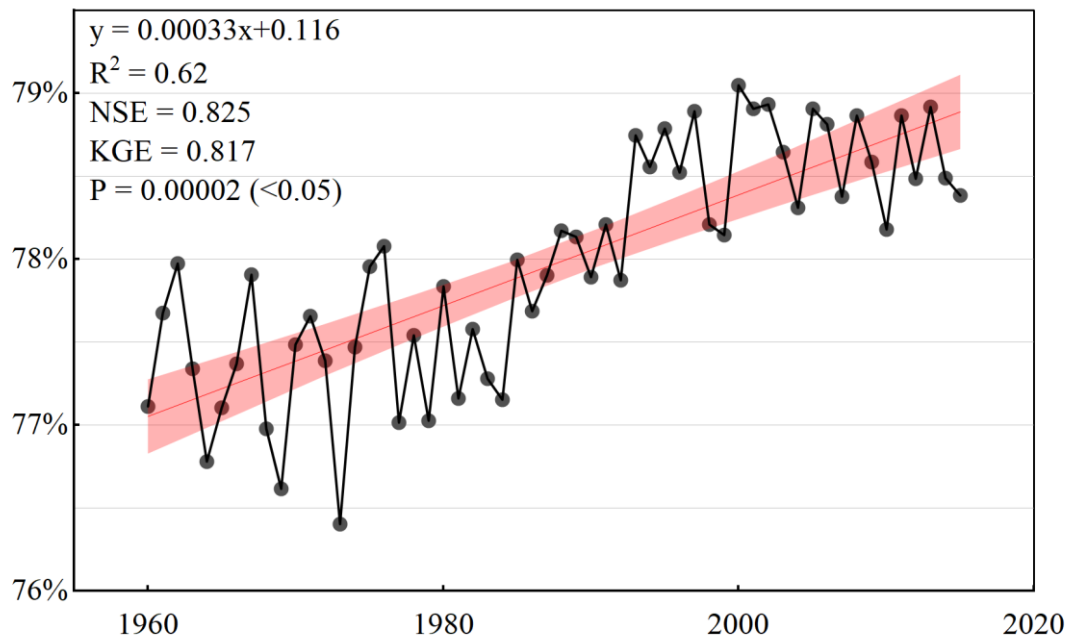
As can be seen from Figure 7, there are differences in the characteristics of BFIs over time in different climatic zones. The BFI in the tropical karst region generally shows an increasing trend. From 1960 to about 1990, the base flow index in tropical karst showed an increasing trend, and since 1990 the base flow index remained at about 80% and then stabilized. The BFI in arid karst region is the highest, with a mean value of about 85%. In general, the BFI in arid karst region shows a decreasing trend, and the annual mean BFI fluctuates greatly, with poor stability. The BFI of subtropical karst region is more stable, always maintained at about 78%. The characteristics of BFI in temperate karst regions are similar to those of tropical karst, showing a slow increase and remaining stable at around 80%.



361

362 Figure 7. Temporal variations of annual BFI for different karst climatic zones compared  
 363 to the global average. The x-axis indicates the year, and the y-axis indicates the BFI  
 364 percentage. The thin colored lines represent the BFI fluctuations in Arid (yellow),  
 365 Tropical (green), Subtropical (teal), and Temperate (purple) karst regions. The dark blue  
 366 line represents the weighted average BFI for all karst regions ("Karst"), while the brown  
 367 curve at the bottom represents the non-Karst average BFI ("non-Karst "). The red  
 368 horizontal line marks the long-term overall mean of the karst BFI (approximately 78%).

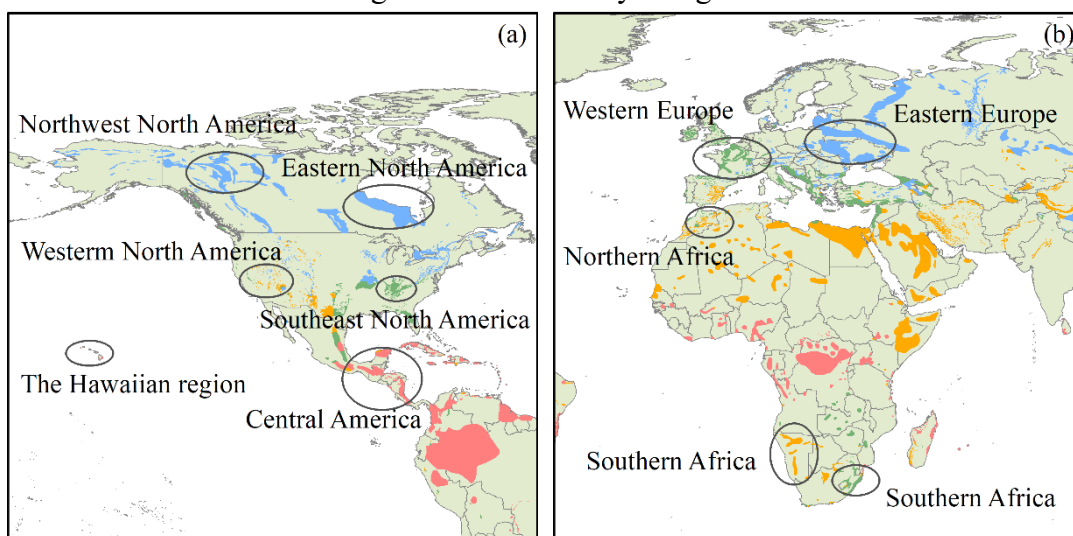
369 The mean Base Flow Index (BFI) derived from four methods (FIM, Boughton,  
 370 Eckhardt, and EWMA) was adopted as the BFI for global karst regions. To quantify the  
 371 trend and its reliability, we calculated the Mann–Kendall test and linear regression  
 372 metrics (Figure 8). The analysis reveals a statistically significant increasing trend in  
 373 BFI ( $P=0.00002<0.05$ ). The model performance metrics— $R^2$  of 0.62, NSE of 0.825,  
 374 and KGE of 0.817—indicate a strong agreement between the fitted trend and observed  
 375 data, despite natural inter-annual fluctuations. The trend suggests an approximate  
 376 increase of 1.5% between 1960 and 2015. A notable rising period occurred from 1980  
 377 to 2000. Since 2000, the BFI in global karst regions has stabilized, fluctuating within a  
 378 range of  $78.5\% \pm 0.5\%$ .



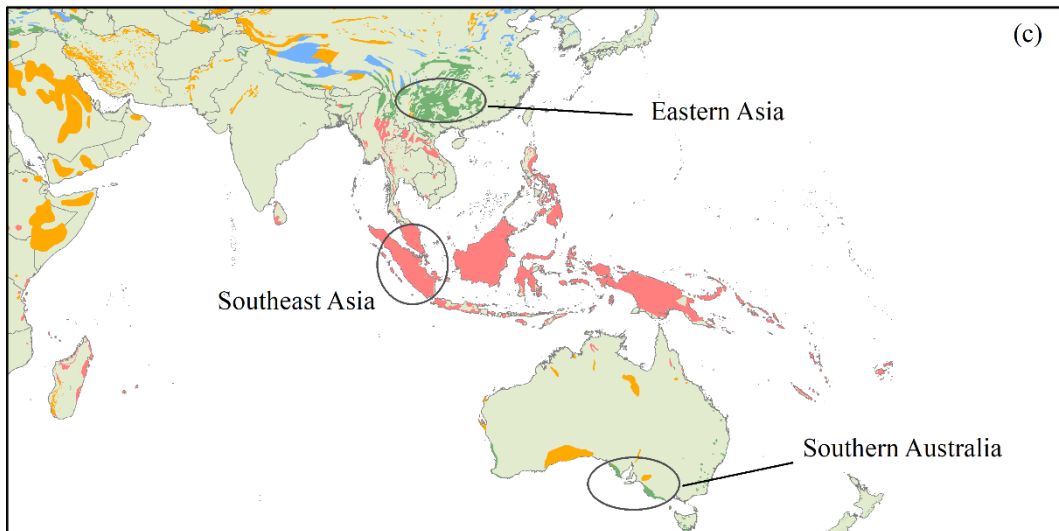
379

380 Figure 8. Annual mean BFIs over time for global karst regions. x-axis indicates year, y-  
 381 axis indicates BFIs, and red bars indicate 95% confidence interval.

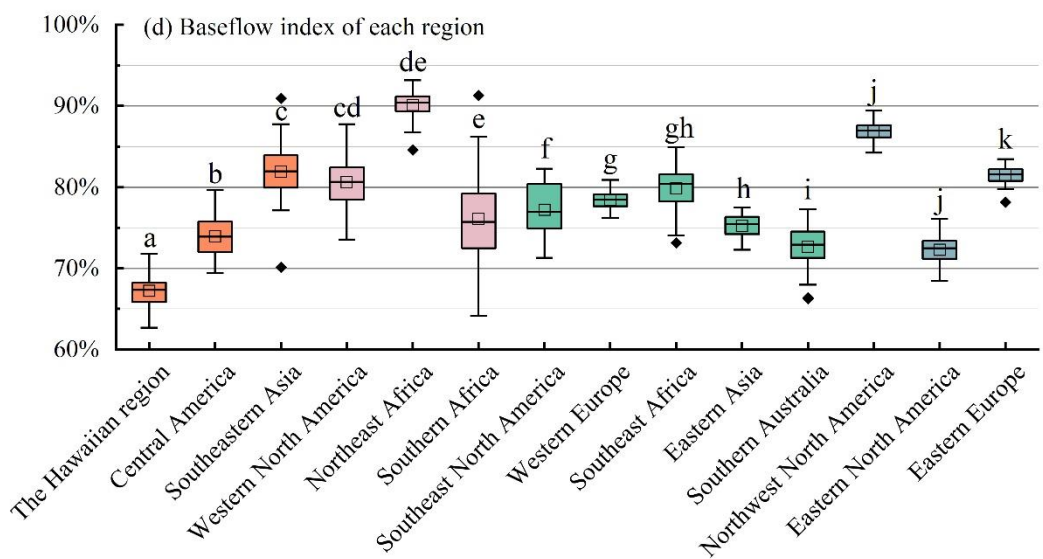
382 Figure 9 shows that, despite being in the same climatic zone, different regions can  
 383 exhibit differences in BFIs. For example, in the northern part of South America and the  
 384 Southeast Asian region, which are both tropical Karst, the BFI is significantly higher in  
 385 the Southeast Asian region (81%) than in the northern part of South America (73%).  
 386 There is also a significant difference in BFIs between the eastern part of the United  
 387 States and the northern part of Africa, which are both arid karst climate zones. From  
 388 figure 9 and figure 10 we find that BFI stability is lower and BFI values are higher in  
 389 arid karst regions. The degree of variation of BFI in tropical karst regions is lower than  
 390 that in arid karst regions. And subtropical and temperate karst regions have the lowest  
 391 trend of base flow index change and their stability is higher.



392

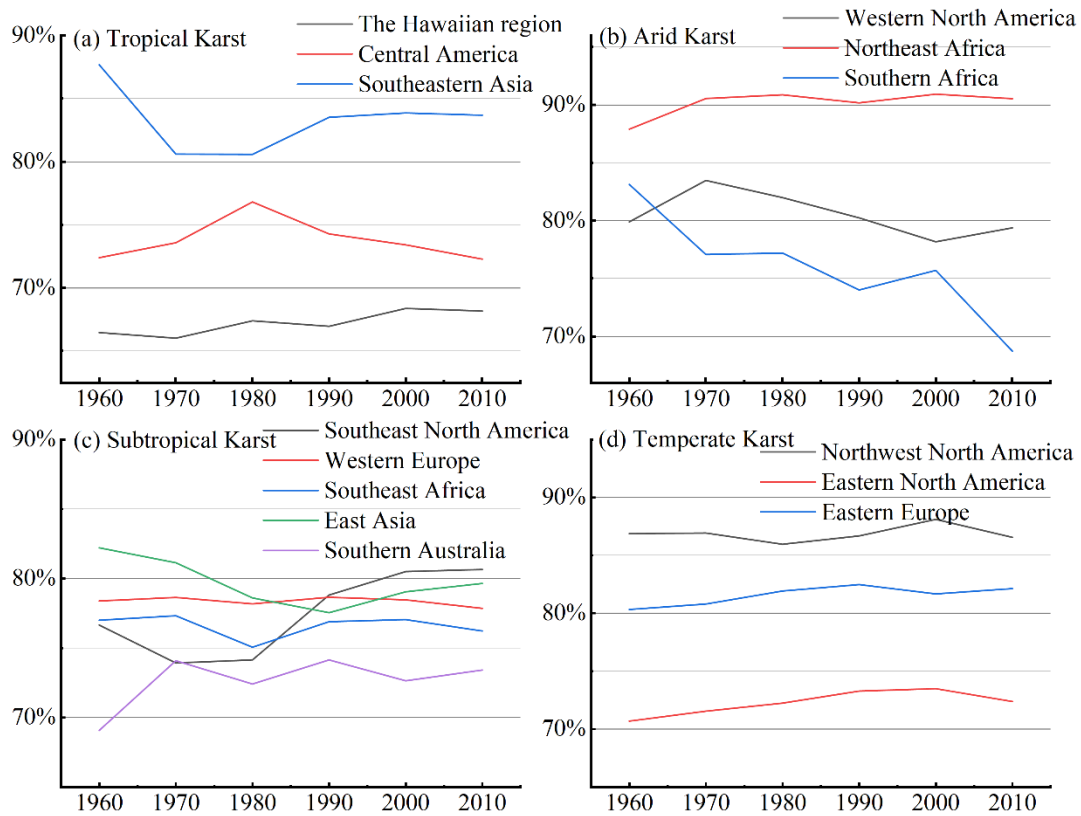


393



394

395 Figure 9. Distribution of BFIs in karst basins in different regions within the same  
 396 climatic zone. In figure (d), orange represents tropical karst regions, magenta represents  
 397 arid karst regions, green bars represent subtropical karst regions, and brownish-purple  
 398 represents temperate karst regions.



399

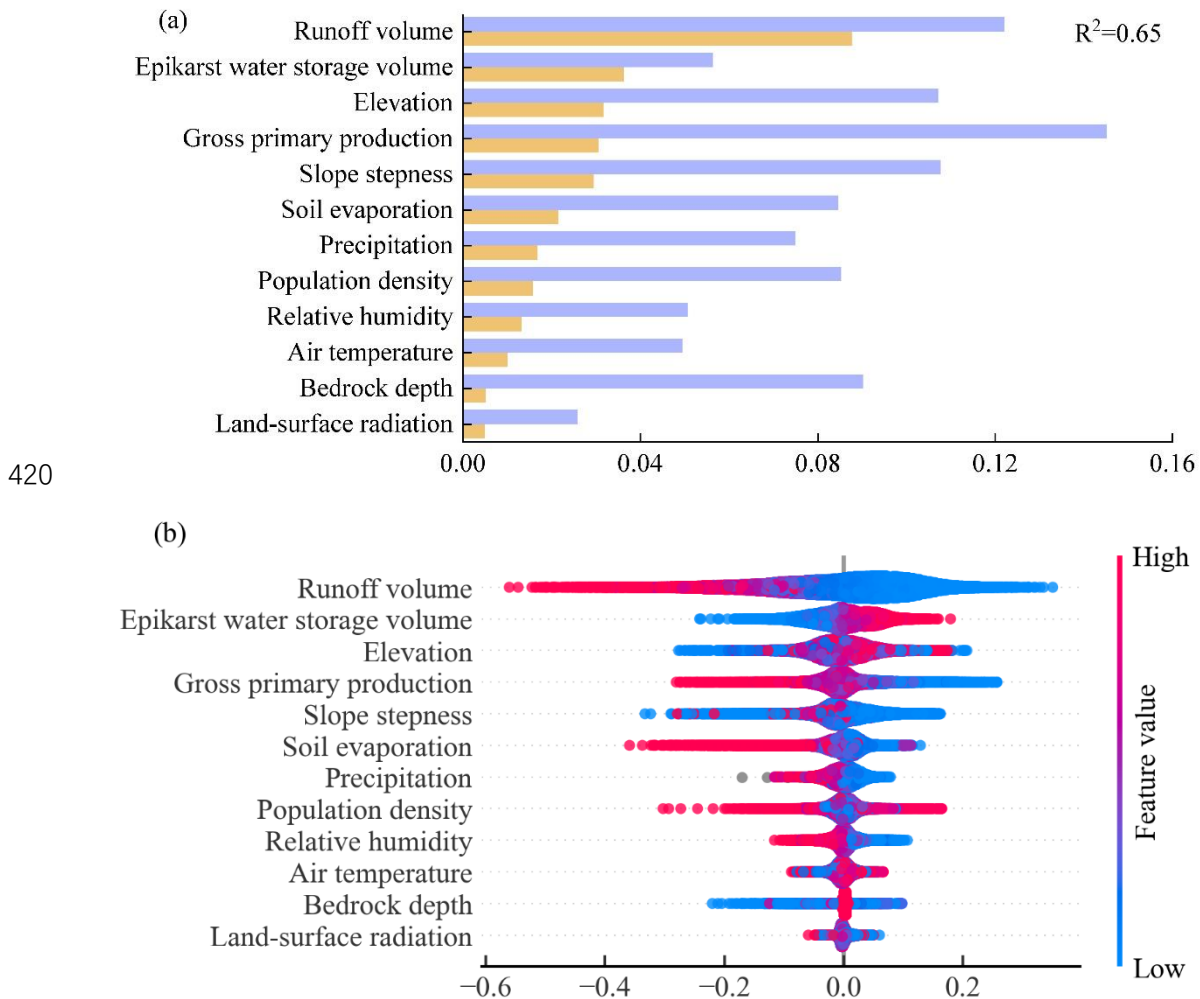
400 Figure 10. Characteristics of BFIs with respect to year for different regions within the  
 401 same climatic zone. Where Y-axis indicates BFI and X-axis indicates year.

### 402 3.4 Factors influencing baseflow indices in karst regions

403 From a global perspective, runoff volume contributes the most to the Baseflow  
 404 Index (BFI) in terms of both XGBoost feature importance and SHAP importance  
 405 (Figure 11a). The influence of other factors on the BFI remains largely consistent  
 406 between the two methods. Notably, however, distinct discrepancies exist between the  
 407 two metrics regarding epikarst water storage volume and bedrock depth. This is likely  
 408 because standard XGBoost importance evaluates features from a model-construction  
 409 perspective (e.g., gain or frequency), whereas SHAP assesses the contribution of  
 410 features to the specific prediction outcomes.

411 From a detailed perspective (Figure 11b), runoff volume and epikarst water storage  
 412 volume are the most stable positive drivers of baseflow; they exhibit high SHAP values,  
 413 where larger feature values correspond to a stronger promoting effect. Population  
 414 density, in contrast, demonstrates a clear inhibitory effect, with high values  
 415 corresponding to significant negative SHAP contributions. Precipitation, serving as a  
 416 recharge factor, also shows a consistent positive influence. Conversely, the directions  
 417 of influence for air temperature and land-surface radiation are unstable, suggesting that

418 their effects are highly context-dependent. The remaining topographic and ecological  
 419 factors have a relatively minor overall impact on baseflow.



421  
 422 Figure 11. Contribution of different factors to baseflow and their characteristic  
 423 distributions. Subfigure (a) illustrates the feature importance derived from XGBOOST  
 424 and SHAP analysis, with  $R^2$  representing the coefficient of determination of the  
 425 XGBOOST model. Subfigure (b) depicts the influence characteristics of various factors  
 426 on the baseflow index, where the horizontal axis indicates the magnitude of values and  
 427 the vertical axis lists the different factor types.

## 428 4. Discussion

### 429 4.1 Mechanisms of formation of baseflow characteristics in karst 430 regions

431 The results of the study show that the BFI in karst regions is significantly higher  
 432 than the global average (Figure 7). We attribute this difference to the unique geological  
 433 structure and hydrological cycle characteristics of karst regions. Extensively developed  
 434 fissures, vertical seepage zones, and subsurface dissolution piping systems in karst

435 regions constitute complex hydrological channels, which significantly alter surface  
436 water-groundwater exchange patterns (Ford & Williams, 2007; Li et al., 2024).  
437 Compared with the homogeneous water storage medium dominated by fissures and  
438 pores in non-karst areas, the network of dissolution channels in karst regions  
439 significantly shortens the infiltration path of precipitation, and its infiltration rate can  
440 reach several to tens of times that of in non-karst areas (Fu et al., 2016). For example,  
441 the monitoring of karst slopes in Huanjiang, Guangxi, shows that the wet front transport  
442 rate is as high as 1373 mm/h, compared with 17-610 mm/h in non-karst regions, which  
443 indicates that the rate of water infiltration in karst regions is much higher than that in  
444 non-karst regions (Medici et al., 2019; Zhang et al., 2024). This part of precipitation  
445 recharge into the subsurface, under the action of gravity and pressure, squeezes the ‘old  
446 water’ out of the underground aquifer, which indirectly enhances the baseflow ratio  
447 (Reimann et al., 2011; Bailly-Comte et al., 2010; Evans, 1983; Ronayne, 2013). Studies  
448 have shown that this mechanism can result in significantly higher baseflow  
449 contributions in karst regions, even above 80% in specific environments (Zhang et al.,  
450 2022), whereas only less than 50% of precipitation can be converted to baseflow in non-  
451 karst regions due to the blocking effect of loose sedimentary layers (Cusano et al., 2024).

452 Significant differences in surface cover conditions further reinforce baseflow  
453 differences. In some karst areas, **bedrock exposure exceeds 60%**, and thin layers of  
454 residual soil (<30 cm) cover only 20% of the surface, a geologic feature that results in  
455 reduced surface interception and elevated subsurface recharge (Anker et al., 2023; Li et  
456 al., 2024; Wang et al., 2024). The karst fissure system is directly exposed to the  
457 atmospheric interface, avoiding water loss through evaporation from the soil layer, and  
458 the lack of continuous surface cover allows for direct infiltration of large amounts of  
459 precipitation (Yang et al., 2025; Li et al., 2023). On the contrary, in non-karst areas, the  
460 soil-vegetation system formed by thicker weathered crust constitutes a natural  
461 evapotranspiration interface, and the average annual evapotranspiration can reach 40%  
462 of the precipitation, and surface runoff accounts for 30% of the precipitation, which  
463 significantly weakened the intensity of groundwater recharge (Jiang et al., 2020; Wang  
464 et al., 2020; Wetzel et al., 1996). This double hydrological barrier effect ultimately leads  
465 to systematic differences between BFIs in karst regions and non-karst regions.

466 **4.2 Reasons for differences in baseflow in karst regions in different**  
467 **climatic zones**

468 The results show that BFIs in karst regions in different climatic zones exhibit  
469 significant differences (Figure 9 and Figure 10). The underlying driving force lies in  
470 the heterogeneity of the geologic structure and its coupling effect with long-term  
471 climatic erosion (Liu et al., 2023). Among them, the control of the spatial structure of  
472 the water storage medium by the geologic context is the decisive factor for the  
473 differences in BFIs (Luo et al., 2023). For example, in Southeast Asian karst regions  
474 (e.g., Halong Bay, Vietnam), due to the development of high-purity, thick-bedded  
475 limestone, and the formation of a pipeline network with vertical dominance under the  
476 background of tectonic uplift, the short groundwater runoff paths and efficient recharge  
477 mechanisms directly enhance the baseflow (Düringer et al., 2012). In contrast, siliceous  
478 interbedding in dolomite formations in northern South America (e.g., Caatinga, Brazil)  
479 significantly increases the resistance to dissolution and reduces the connectivity of the  
480 dissolution network, a primary geologic feature that fundamentally constrains the  
481 baseflow (Teixeira et al., 2023). The intensity of tectonic activity and the stage of  
482 geomorphic evolution further strengthen regional differences. For example, strong  
483 Cenozoic uplift in Southeast Asia formed steep young landforms that promoted vertical  
484 permeability dominance. In contrast, Paleozoic stable landmasses in northern Africa  
485 (e.g., the Saharan Atlas Mountains) are dominated by horizontal cave systems, a  
486 geologic feature that also distinguishes the baseflow in this region from that in other  
487 regions (Klimchouk, 2007; Jiang et al., 2020). Surface cover characteristics are equally  
488 critical as secondary geologic elements. For example, thicker soil layers in temperate  
489 zones (e.g., Slovenia) increase surface runoff diversion through delayed infiltration,  
490 whereas large areas of exposed bedrock in equatorial zones allow precipitation to  
491 infiltrate directly through solution gaps, creating a multiplicative effect on the BFI (Li  
492 et al., 2023).

493 Climate elements reshape geological structures over large time scales through  
494 geological erosion processes, thereby indirectly influencing baseflow patterns. While  
495 short-term hydrological dynamics are affected by climate parameters such as  
496 precipitation intensity and seasonal distribution (Mo et al., 2021; Cheng et al., 2023),  
497 the profound control of climate on the baseflow index is evident in its long-term  
498 modification of karst systems. For example, the strong coupling of heavy precipitation  
499 and high temperatures in equatorial regions significantly accelerates the dissolution of  
500 carbonate rocks, forming a dense network of highly permeable dissolution fissures.  
501 Conversely, the persistent moisture associated with temperate maritime climates

502 enhances the dissolution of carbonate rocks (with an average annual dissolution rate  
503 approximately 40% higher than that of non-karst areas at the same latitude), leading to  
504 the formation of cave clusters characterized by labyrinthine structures and interwoven  
505 underground river systems. This climate-driven differentiation in dissolution alters the  
506 capacity of groundwater storage spaces, ultimately being reflected in the characteristic  
507 values of regional baseflow indices (Ford and Williams, 2007; Goldscheider, 2015;  
508 Tapiador et al., 2012).

#### 509 4.3 Reasons for changes in baseflow indices over time

510 The results of the analysis revealed an increasing trend in the BFI in the karst  
511 region (Figure 8). Although the degree of increase is low (about 1.5% from 1960 to  
512 2015), we still consider this degree of increase in BFI noteworthy given that the average  
513 BFI in the karst region is already at a high level. This increasing trend in BFI in the  
514 karst region is presumably driven by substantial groundwater loss. Extensive  
515 monitoring has shown that groundwater levels globally show a rapid declining trend,  
516 and this systematic depletion has triggered multiple crises such as basin hydrological  
517 process anomalies and regional climate feedback imbalances (Jasechko et al., 2024, de  
518 Graaf et al. 2019; Liu et al.,2015). It is the rapid decline of the water table that leads to  
519 a constant unsaturated state of groundwater storage. Therefore, when recharged by  
520 precipitation, large amounts of precipitation preferentially replenish the storage deficits,  
521 making the generation of surface runoff more difficult and delayed.

522 In addition to this, the geological and hydrological characteristics of the karst  
523 region further amplify this effect of reduced surface runoff and increased baseflow (Zhu  
524 et al.,2025). On the one hand, there is the rapid water-conducting effect of the karst  
525 fissure network, where the extensive development of dissolution pipes and fissures in  
526 the karst bedrock accelerates vertical infiltration of precipitation into deep groundwater,  
527 leading to difficulties in retaining soil moisture and a significant increase in the runoff  
528 generation threshold (Hartmann et al., 2014). On the other hand, there is the dissipative  
529 effect of the surface-subsurface dichotomy, where the thickness of the unsaturated zone  
530 of the karst aquifer increases in the context of persistent groundwater overdraft  
531 (D'Ettorre et al., 2024), further weakening the immediate contribution of precipitation  
532 events to runoff.

#### 533 4.4 Applicability and limitations of this study

534 Regarding data sources, the datasets used are inherently diverse and complex.

535 Although substantial efforts were made to exclude studies with distorted data and screen  
536 out unreasonable values during calculation, it remains challenging to fully eliminate  
537 inherent deficiencies in the original datasets.

538 There are also limitations regarding the applicability of the methods themselves.  
539 For example, the parameterization framework of digital filtering methods (e.g.,  
540 Eckhardt and Chapman algorithms) based on the assumption of linear recession is at  
541 variance with the nonlinear characteristics of karst hydrological processes. Furthermore,  
542 the rapid recession processes dominated by karst pipe flow (rates up to 2-3 times those  
543 of porous media basins) lead to a general underestimation of the recession coefficient  
544 (Kang et al., 2022; Rattayová & Hlavčová, 2023), which leads to differences in  
545 baseflow separation between methods with different principles. For instance, the  
546 baseflow separation results yielded by the Chapman and CM methods in this study are  
547 significantly lower than those of other methods. This discrepancy arises because these  
548 methods are less responsive to precipitation recharge, a finding consistent with Helfer  
549 et al. (2024). In addition, empirical parameters such as maximum baseflow (BFI\_max)  
550 are mostly derived from calibration results in temperate homogeneous aquifers, and  
551 their physical mechanisms have not been fully adapted for applicability in karst regions  
552 (Zhou et al., 2017).

553 Despite the above limitations, this study ensures the spatial representativeness and  
554 methodological reliability of the conclusions by integrating a global-scale multi-source  
555 dataset of karst regions (covering more than 85% of the typical karst geomorphological  
556 units) and adopting standardized validation indexes (KGE, NSE). The findings  
557 demonstrate that the applied baseflow separation techniques can effectively  
558 characterize the regional hydrological features and provide data support for water  
559 resource management and eco-hydrological model construction in karst regions. Future  
560 research can integrate geophysical exploration and isotope tracer technology to develop  
561 a dynamic parameterization scheme adapted to non-homogeneous media.

## 562 5. Conclusion

563 This study systematically analyzes the spatial distribution characteristics and trends  
564 of BFIs in global karst regions. The results show that the BFI (78%) in karst regions is  
565 generally significantly higher than the global average. This phenomenon confirms the  
566 differential regulation of the runoff partitioning mechanism by the unique surface-  
567 groundwater dichotomy in karst regions. Meanwhile, the study systematically evaluates  
568 the applicability limits of hydrograph separation methods in karst regions and

569 demonstrates their effectiveness. It is noteworthy that the BFI in karst regions shows a  
570 phased upward trend in the context of global groundwater depletion. This may be  
571 related to the buffering effect of karst aquifers on extreme climatic events and human  
572 activity-induced changes in subsurface storage conditions. Future research should  
573 integrate high-precision geological tectonic data and multi-source remote sensing  
574 information to construct a coupled climate-hydrology-geology model. This will allow  
575 for quantitative analysis of the response characteristics of hydrological fluxes of karst  
576 systems in the context of climate change, and further improve the spatiotemporal  
577 understanding of the karst water cycle.

578

## 579 Declaration of the Competing Interest

580 The authors declare that they have no known competing financial interests or  
581 personal relationships that could have appeared to influence the work reported in this  
582 paper

## 583 Acknowledgments

584 This study was supported by the National Natural Science Foundation of China  
585 (42461004, U1812401, U1612441); Science and Technology Plan Project of Guizhou  
586 Province (Qiankehejichu-ZK[2025] Zhongdian 045; Qiankehejichu-ZK[2025]  
587 Mianshang 268)  
588

## 589 References:

- 590 Mukherjee, A., Bhanja, S.N. & Wada, Y. Groundwater depletion causing reduction of baseflow  
591 triggering Ganges river summer drying. *Sci Rep* **8**, 12049 (2018). [https://doi.org/10.1038/s41598-](https://doi.org/10.1038/s41598-018-30246-7)  
592 [018-30246-7](https://doi.org/10.1038/s41598-018-30246-7)
- 593 Chen, H., Chen, Y., Li, W., & Li, Z. (2019). Quantifying the contributions of snow/glacier meltwater  
594 to river runoff in the Tianshan Mountains, Central Asia. *Global and Planetary Change*, *174*, 47-57.  
595 <https://doi.org/10.1016/j.gloplacha.2019.01.002>
- 596 Saedi, J., Sharifi, M.R., Saremi, A. *et al.* Assessing the impact of climate change and human activity  
597 on streamflow in a semiarid basin using precipitation and baseflow analysis. *Sci Rep* **12**, 9228  
598 (2022). <https://doi.org/10.1038/s41598-022-13143-y>
- 599 Hare, D.K., Helton, A.M., Johnson, Z.C. *et al.* Continental-scale analysis of shallow and deep  
600 groundwater contributions to streams. *Nat Commun* **12**, 1450 (2021).  
601 <https://doi.org/10.1038/s41467-021-21651-0>
- 602 Yang, C., Condon, L.E. & Maxwell, R.M. Unravelling groundwater–stream connections over the  
603 continental United States. *Nat Water* **3**, 70–79 (2025). <https://doi.org/10.1038/s44221-024-00366-8>
- 604 Zhang, J., Song, J., Cheng, L., Zheng, H., Wang, Y., Huai, B., Sun, W., Qi, S., Zhao, P., Wang, Y., &  
605 Li, Q. (2019). Baseflow estimation for catchments in the Loess Plateau, China. *Journal of*  
606 *Environmental Management*, *233*, 264-270. <https://doi.org/10.1016/j.jenvman.2018.12.040>
- 607 Mei, Y., Wang, D., Zhu, J., Tang, G., Cai, C., Shen, X., et al. (2024). Optimal baseflow separation  
608 through chemical mass balance: Comparing the usages of two tracers, two concentration estimation  
609 methods, and four baseflow filters. *Water Resources Research*, *60*,  
610 e2023WR036386. <https://doi.org/10.1029/2023WR036386>
- 611 Kuehne, L. M., Dickens, C., Tickner, D., Messenger, M. L., Olden, J. D., O'Brien, G., Lehner, B., &  
612 Eriyagama, N. (2023). The future of global river health monitoring. *PLOS Water*, *2*(9), 1-27. Article  
613 e0000101. <https://doi.org/10.1371/journal.pwat.0000101>
- 614 Xie, J., Liu, X., Jasechko, S. *et al.* Majority of global river flow sustained by groundwater. *Nat.*  
615 *Geosci.* **17**, 770–777 (2024). <https://doi.org/10.1038/s41561-024-01483-5>
- 616 Beck, H. E., A. I. J. M. van Dijk, D. G. Miralles, R. A. M. de Jeu, L. A. Bruijnzeel, T. R. McVicar,  
617 and J. Schellekens (2013), Global patterns in base flow index and recession based on streamflow  
618 observations from 3394 catchments, *Water Resour. Res.*, *49*, 7843–7863,  
619 doi:10.1002/2013WR013918.

620 Lyu, S., Guo, C., Zhai, Y., Huang, M., Zhang, G., Zhang, Y., Cheng, L., Liu, Q., Zhou, Y., Woods,  
621 R., Zhang, J., & 11 others. (2023). Characterising baseflow signature variability in the Yellow River  
622 Basin. *Journal of Environmental Management*, 345, 118565.  
623 <https://doi.org/10.1016/j.jenvman.2023.118565>

624 Zhang, J., Song, J., Cheng, L., Zheng, H., Wang, Y., Huai, B., ... & Li, Q. (2019). Baseflow  
625 estimation for catchments in the Loess Plateau, China. *Journal of environmental management*, 233,  
626 264-270.

627 Zhang, J., Song, J., Cheng, L., Zheng, H., Wang, Y., Huai, B., ... & Li, Q. (2019). Baseflow  
628 estimation for catchments in the Loess Plateau, China. *Journal of Environmental Management*, 233,  
629 264-270. <https://doi.org/10.1016/j.jenvman.2018.12.040>

630 Jing, J., Li, R., Xiao, L., Shu, D., & Yang, P. (2024). Interpreting and modelling the daily extreme  
631 sediment events in karst mountain watersheds. *Science of The Total Environment*, 926, 171956.  
632 <https://doi.org/10.1016/j.scitotenv.2024.171956>

633 Ford, D., & Williams, P. (2007). *karst Hydrogeology and Geomorphology*. John Wiley & Sons Ltd.  
634 <https://doi.org/10.1002/9781118684986>

635 Medici, G., Munn, J.D. & Parker, B.L. Delineating aquitard characteristics within a Silurian  
636 dolostone aquifer using high-density hydraulic head and fracture datasets. *Hydrogeol J* **32**, 1663–  
637 1691 (2024). <https://doi.org/10.1007/s10040-024-02824-9>

638 Giese, M., Reimann, T., Bailly-Comte, V., Maréchal, J.-C., Sauter, M., & Geyer, T. (2018).  
639 Turbulent and laminar flow in karst conduits under unsteady flow conditions: Interpretation of  
640 pumping tests by discrete conduit-continuum modeling. *Water Resources Research*, 54, 1918–1933.  
641 <https://doi.org/10.1002/2017WR020658>

642 Rosmalinda Permatasari, Arwin Sabar, Dantje Kardana Natakusumah, & Hazairin Samaulah. (2019).  
643 EFFECTS OF WATERSHED TOPOGRAPHY AND LAND USE ON BASEFLOW  
644 HYDROLOGY IN UPSTREAM KOMERING SOUTH SUMATERA, INDONESIA. *GEOMATE*  
645 *Journal*, 17(59), 28–33. Retrieved from <https://geomatejournal.com/geomate/article/view/251>

646 Khomsati, N. L., Suryoputro, N., Yulistyorini, A., Idfi, G., & Alias, N. E. B. (2021). The effect of  
647 forest area change in tropical islands towards baseflow and streamflow. *IOP Conference Series:*  
648 *Earth and Environmental Science*, 847, 012032. <https://doi.org/10.1088/1755-1315/847/1/012032>

649 Longobardi A, Van Loon AF. Assessing baseflow index vulnerability to variation in dry spell length  
650 for a range of catchment and climate properties. *Hydrological Processes*. 2018; 32: 2496–  
651 2509. <https://doi.org/10.1002/hyp.13147>

652 Guisiano, P. A., Santoni, S., Huneau, F., Mattei, A., & Garel, E. (2024). Using natural tracers and  
653 calibrated analytical filter to highlight baseflow contribution to mountainous Mediterranean rivers  
654 in a context of climate change. *Journal of Hydrology*, 641, 131842.  
655 <https://doi.org/10.1016/j.jhydrol.2024.131842>

656 Mo, C., Ruan, Y., Xiao, X., Lan, H., & Jin, J. (2021). Impact of climate change and human activities  
657 on the baseflow in a typical karst basin, Southwest China. *Ecological Indicators*, 126, 107628.  
658 <https://doi.org/10.1016/j.ecolind.2021.107628>

659 Luo, Y., Zhou, Q., Peng, D., Yan, W., & Zhao, M. (2023). Key influence of hydrogeological,  
660 geochemical, and geological structure factors on runoff characteristics in karst catchments. *Journal*  
661 *of Hydrology*, 623, 129852. <https://doi.org/10.1016/j.jhydrol.2023.129852>

662 Li, Y., Zhou, Q. & Zhao, Y. Hydrologic response in a typical karst desertification catchment.  
663 *Carbonates Evaporites* 39, 16 (2024). <https://doi.org/10.1007/s13146-024-00929-6>

664 Li, Y., Li, K., Zhou, Q., Zhao, Y., Cai, L., & Yang, Z. (2024). Spatiotemporal dynamics and similarity  
665 in soil moisture in shallow soils on karst slopes. *Journal of Hydrology*, 639, 131655.  
666 <https://doi.org/10.1016/j.jhydrol.2024.131655>

667 Zhu De-gen, Ning Jing, Yang Hui, Pu Jun-bing, Cao Jian-hua, Zhou Meng-xia, Prelovšek Mitja,  
668 Ravbar Nataša. 2025. Research hotspot and trend of plant water use in karst: Based on a bibliometric  
669 analysis from 1984 to 2022. *China Geology*, 8(1), 214–229. doi: 10.31035/cg2023134.

670 Cheng, S., Yu, X., Li, Z., Xu, X., Gao, H., & Ye, Z. (2023). The effect of climate and vegetation  
671 variation on monthly sediment load in a karst watershed. *Journal of Cleaner Production*, 382\*,  
672 135290. <https://doi.org/10.1016/j.jclepro.2022.135290>

673

674 Tobin BW, Schwartz BF. Quantifying the role of karstic groundwater in a snowmelt-dominated  
675 hydrologic system. *Hydrological Processes*. 2020; 34: 3439–  
676 3447. <https://doi.org/10.1002/hyp.13833>

677 Tobin BW, Schwartz BF. Quantifying the role of karstic groundwater in a snowmelt-dominated  
678 hydrologic system. *Hydrological Processes*. 2020; 34: 3439–  
679 3447. <https://doi.org/10.1002/hyp.13833>

680 Mo, C., Jiang, C., Long, S., & Cen, W. (2025). Comprehensive evaluation and attribution analysis  
681 of baseflow variation in a typical karst basin, Southwest China. *Journal of Hydrology: Regional  
682 Studies*, 57, 102185. <https://doi.org/10.1016/j.ejrh.2025.102185>

683 Foran Quinn, D., Murphy, C., Wilby, R. L., Matthews, T., Broderick, C., Golian, S., ... Harrigan, S.  
684 (2021). Benchmarking seasonal forecasting skill using river flow persistence in Irish  
685 catchments. *Hydrological Sciences Journal*, 66(4), 672–688.  
686 <https://doi.org/10.1080/02626667.2021.1874612>

687 Lyu, S., Zhai, Y., Zhang, Y., Cheng, L., Paul, P. K., Song, J., Wang, Y., Huang, M., Fang, H., &  
688 Zhang, J. (2022). Baseflow signature behaviour of mountainous catchments around the North China  
689 Plain. *Journal of Hydrology*, 606, 127450. <https://doi.org/10.1016/j.jhydrol.2022.127450>

690 Tagne, G. V. and Dowling, C., "Inferring groundwater flow and recharge from time series analysis  
691 of storm responses in a karst aquifer of southeastern Kentucky (USA)" (2018). KIP Articles.  
692 2659. [https://digitalcommons.usf.edu/kip\\_articles/2659](https://digitalcommons.usf.edu/kip_articles/2659)

693 Guisiano, P. A., Santoni, S., Huneau, F., Mattei, A., & Garel, E. (2024). Using natural tracers and  
694 calibrated analytical filter to highlight baseflow contribution to mountainous Mediterranean rivers  
695 in a context of climate change. *Journal of Hydrology*, 641, 131842.  
696 <https://doi.org/10.1016/j.jhydrol.2024.131842>

697 He, Z., Unger-Shayesteh, K., Vorogushyn, S., Weise, S. M., Kalashnikova, O., Gafurov, A.,  
698 Duethmann, D., Barandun, M., & Merz, B. (2019). Constraining hydrological model parameters  
699 using water isotopic compositions in a glacierized basin, Central Asia. *Journal of Hydrology*, 571,  
700 332-348. <https://doi.org/10.1016/j.jhydrol.2019.01.048>

701 Yang, Y., Weng, B., Yan, D., Gong, X., Dai, Y., Niu, Y., & Dong, G. (2021). Tracing potential water  
702 sources of the Nagqu River using stable isotopes. *Journal of Hydrology: Regional Studies*, 34,  
703 100807. <https://doi.org/10.1016/j.ejrh.2021.100807>

704 Arnold, Jeffrey G. et al. "SWAT: Model Use, Calibration, and Validation." *Transactions of the  
705 ASABE* 55 (2012): 1491-1508.

706 Wu, L., Wang, S., Bai, X., Luo, W., Tian, Y., Zeng, C., Luo, G., & He, S. (2017). Quantitative  
707 assessment of the impacts of climate change and human activities on runoff change in a typical karst

708 watershed, SW China. *Science of The Total Environment*, 601–602, 1449-1465.  
709 <https://doi.org/10.1016/j.scitotenv.2017.05.288>

710 Lehner, B., Grill G. (2013). Global river hydrography and network routing: baseline data and new  
711 approaches to study the world’s large river systems. *Hydrological Processes*, 27(15): 2171–  
712 2186. <https://doi.org/10.1002/hyp.9740>

713 Li, Bailing, Rodell, Matthew, Sheffield, Justin, Wood, Eric, Sutanudjaja, Edwin. 2019. Long-term,  
714 non-anthropogenic groundwater storage changes simulated by three global-scale hydrological  
715 models. *Scientific Reports*. Vol. 9, No. 1, pp. 10746. DOI: 10.1038/s41598-019-47219-  
716 z ISSN: 2045-2322

717 Hengl, T., Mendes de Jesus, J., Heuvelink, G. B., Ruiperez Gonzalez, M., Kilibarda, M., Blagotić,  
718 A., Shanguan, W., Wright, M. N., Geng, X., Bauer-Marschallinger, B., Guevara, M. A., Vargas, R.,  
719 MacMillan, R. A., Batjes, N. H., Leenaars, J. G., Ribeiro, E., Wheeler, I., Mantel, S., & Kempen, B.  
720 (2017). SoilGrids250m: Global gridded soil information based on machine learning. *PloS one*, 12(2),  
721 e0169748. <https://doi.org/10.1371/journal.pone.0169748>

722 arris, I., Osborn, T.J., Jones, P. *et al.* Version 4 of the CRU TS monthly high-resolution gridded  
723 multivariate climate dataset. *Sci Data* 7, 109 (2020).

724 Fick, S.E. and R.J. Hijmans, 2017. WorldClim 2: new 1km spatial resolution climate surfaces for  
725 global land areas. *International Journal of Climatology* 37 (12): 4302-4315.

726 Wieder, W.R., J. Boehnert, G.B. Bonan, and M. Langseth. 2014. RegridDED Harmonized World Soil  
727 Database v1.2. ORNL DAAC, Oak Ridge, Tennessee, USA.  
728 <https://doi.org/10.3334/ORNLDAAC/1247>

729 Bright, E., Rose, A., & Urban, M. (2013). *LandScan Global 2012* [Data set]. Oak Ridge National  
730 Laboratory. <https://doi.org/10.48690/1524215>

731 Wild, B., Teubner, I., Moesinger, L., Zotta, R.-M., Forkel, M., van der Schalie, R., Sitch, S., and  
732 Dorigo, W.: VODCA2GPP – a new, global, long-term (1988–2020) gross primary production dataset  
733 from microwave remote sensing, *Earth Syst. Sci. Data*, 14, 1063–1085, [https://doi.org/10.5194/essd-](https://doi.org/10.5194/essd-14-1063-2022)  
734 14-1063-2022, 2022.

735 Tang, W. (2019). Dataset of high-resolution (3 hour, 10 km) global surface solar radiation (1983–  
736 2018). National Tibetan Plateau / Third Pole Environment Data  
737 Center. <https://doi.org/10.11888/Meteoro.tpdc.270112>.

738 Brutsaert, W. (2008), Long-term groundwater storage trends estimated from streamflow records:  
739 Climatic perspective, *Water Resour. Res.*, 44, W02409, doi:10.1029/2007WR006518.

740 Rammal, M., Archambeau, P., Erpicum, S., Orban, P., Brouyère, S., Piroton, M.,  
741 & Dewals, B. (2018). Technical note: An operational implementation of recursive digital filter for  
742 base flow separation. *Water Resources Research*, 54, 8528–  
743 8540. <https://doi.org/10.1029/2018WR023351>

744 Xie, J., Liu, X., Wang, K., Yang, T., Liang, K., & Liu, C. (2020). Evaluation of typical methods for  
745 baseflow separation in the contiguous United States. *Journal of Hydrology*, 583, 124628.  
746 <https://doi.org/10.1016/j.jhydrol.2020.124628>

747 Nash, J. E., & Sutcliffe, J. V. (1970). River flow forecasting through conceptual models part I — A  
748 discussion of principles. *Journal of Hydrology*, 10(3), 282-290. [https://doi.org/10.1016/0022-](https://doi.org/10.1016/0022-1694(70)90255-6)  
749 1694(70)90255-6

750 Gupta, H. V., Kling, H., Yilmaz, K. K., & Martinez, G. F. (2009). Decomposition of the mean  
751 squared error and NSE performance criteria: Implications for improving hydrological modelling.

752 Journal of Hydrology, 377(1–2), 80-91. <https://doi.org/10.1016/j.jhydrol.2009.08.003>

753 Niazkar, M., Menapace, A., Brentan, B., Piraei, R., Jimenez, D., Dhawan, P., & Righetti, M. (2024).  
754 Applications of XGBoost in water resources engineering: A systematic literature review (Dec 2018–  
755 May 2023). *Environmental Modelling & Software*, 174, 105971.

756 Zhang, J., Ma, X., Zhang, J., Sun, D., Zhou, X., Mi, C., & Wen, H. (2023). Insights into geospatial  
757 heterogeneity of landslide susceptibility based on the SHAP-XGBoost model. *Journal of*  
758 *Environmental Management*, 332, 117357. <https://doi.org/10.1016/j.jenvman.2023.117357>

759 Chen, Tianqi & Guestrin, Carlos. (2016). XGBoost: A Scalable Tree Boosting System. 785-794.  
760 10.1145/2939672.2939785.

761 Medici, G., West, L. J., & Banwart, S. A. (2019). Groundwater flow velocities in a fractured  
762 carbonate aquifer-type: Implications for contaminant transport. *Journal of Contaminant Hydrology*,  
763 222, 1-16. <https://doi.org/10.1016/j.jconhyd.2019.02.001>

764 Zhang, J., Wang, S., Fu, Z., Wang, K., & Chen, H. (2024). Characterizing rapid infiltration processes  
765 on complex hillslopes: Insights from soil moisture response to rainfall events. *Journal of Hydrology*,  
766 644, 132110. <https://doi.org/10.1016/j.jhydrol.2024.132110>

767 Reimann, T., T. Geyer, W. B. Shoemaker, R. Liedl, and M. Sauter (2011), Effects of dynamically  
768 variable saturation and matrix-conduit coupling of flow in karst aquifers, *Water Resour. Res.*, 47,  
769 W11503, doi:10.1029/2011WR010446.

770 Reimann, T., T. Geyer, W. B. Shoemaker, R. Liedl, and M. Sauter (2011), Effects of dynamically  
771 variable saturation and matrix-conduit coupling of flow in karst aquifers, *Water Resour. Res.*, 47,  
772 W11503, doi:10.1029/2011WR010446.

773 Bailly-Comte, V., Martin, J. B., Jourde, H., Sreaton, E. J., Pistre, S., & Langston, A. (2010). Water  
774 exchange and pressure transfer between conduits and matrix and their influence on hydrodynamics  
775 of two karst aquifers with sinking streams. *Journal of Hydrology*, 386(1-4), 55-66.  
776 <https://doi.org/10.1016/j.jhydrol.2010.03.005>

777 Evans, G. V. (1983). Tracer techniques in hydrology. *The International Journal of Applied Radiation*  
778 *and Isotopes*, 34(1), 451-475. [https://doi.org/10.1016/0020-708X\(83\)90144-8](https://doi.org/10.1016/0020-708X(83)90144-8)

779 Ronayne, M. J. (2013). Influence of conduit network geometry on solute transport in karst aquifers  
780 with a permeable matrix. *Advances in Water Resources*, 56, 27-34.  
781 <https://doi.org/10.1016/j.advwatres.2013.03.002>

782 Zhang, J., Wang, S., Fu, Z., Chen, H., & Wang, K. (2022). Soil thickness controls the rainfall-runoff  
783 relationship at the karst hillslope critical zone in southwest China. *Journal of Hydrology*, 609,  
784 127779. <https://doi.org/10.1016/j.jhydrol.2022.127779>

785 Cusano, D., Allocca, V., Coda, S., Di Clemente, E., Fabbrocino, S., Lepore, D., Panza, R., Petrone,  
786 P., & De Vita, P. (2024). Effects of ash-fall pyroclastic soil mantle on groundwater recharge of  
787 Terminio Mt. peri-volcanic karst aquifer. *Journal of Hydrology: Regional Studies*, 53, 101844.  
788 <https://doi.org/10.1016/j.ejrh.2024.101844>

789 Anker Y, Gimburg A, Zilberbrand M, Livshitz Y, Mirlas V. Groundwater Recharge Assessment for  
790 Small karstic Catchment Basins with Different Extents of Anthropogenic  
791 Development. *Environments*. 2023; 10(9):158. <https://doi.org/10.3390/environments10090158>

792 LI Zhenhua, LI Songtao, DU Feng, *et al.* Research on the development law of karst caves on  
793 water conducting fractures under the influence of mining in Southwest karst Mining Areas[J]. *Coal*  
794 *Science and Technology*, 2023, 51 (7): 106–117. DOI: 10.13199/j.cnki.cst.2023-0409

795 Jiang, Z., Liu, H., Wang, H. *et al.* Bedrock geochemistry influences vegetation growth by regulating

796 the regolith water holding capacity. *Nat Commun* **11**, 2392 (2020). [https://doi.org/10.1038/s41467-](https://doi.org/10.1038/s41467-020-16156-1)  
797 020-16156-1

798 Wang, F., Chen, H., Lian, J., Fu, Z., & Nie, Y. (2020). Hydrological response of karst stream to  
799 precipitation variation recognized through the quantitative separation of runoff components. *Science*  
800 of The Total Environment, 748, 142483. <https://doi.org/10.1016/j.scitotenv.2020.142483>

801 Wetzel, P. J., Liang, X., Irannejad, P., Boone, A., Noilhan, J., Shao, Y., Skelly, C., Xue, Y., & Yang,  
802 Z. L. (1996). Modeling vadose zone liquid water fluxes: Infiltration, runoff, drainage,  
803 interflow. *Global and Planetary Change*, 13(1–4), 57–71. [https://doi.org/10.1016/0921-](https://doi.org/10.1016/0921-8181(95)00037-2)  
804 8181(95)00037-2

805 Düringer, P., Bacon, A.-M., Sayavongkhamdy, T., & Nguyen, T. K. T. (2012). karst development,  
806 breccias history, and mammalian assemblages in Southeast Asia: A brief review. *Comptes Rendus*  
807 *Palevol*, 11(2–3), 133-157. <https://doi.org/10.1016/j.crpv.2011.07.003>

808 Jiang, Z., Liu, H., Wang, H. *et al.* Bedrock geochemistry influences vegetation growth by regulating  
809 the regolith water holding capacity. *Nat Commun* **11**, 2392 (2020). [https://doi.org/10.1038/s41467-](https://doi.org/10.1038/s41467-020-16156-1)  
810 020-16156-1

811 Teixeira, G. M., de Paula, R. S., Velasquez, L. N. M., Andrade, I. B., & Neto, W. M.  
812 P. (2023). Evaluation of recharge estimation methods applied to fissure and karst aquifers of the  
813 Lagoa Santa karst Environmental Protection Area, Brazil. *Hydrological Processes*, 37(8),  
814 e14971. <https://doi.org/10.1002/hyp.14971>

815 Klimchouk, Alexander Borisovich, "Hypogene speleogenesis: Hydrogeological and Morphogenetic  
816 Perspective NCKRI - Special Paper 1" (2007). *KIP Monographs*.  
817 13. [https://digitalcommons.usf.edu/kip\\_monographs/13](https://digitalcommons.usf.edu/kip_monographs/13)

818 Jiang, G., Chen, Z., Siripornpibul, C. *et al.* The karst water environment in Southeast Asia:  
819 characteristics, challenges, and approaches. *Hydrogeol J* **29**, 123–135 (2021).  
820 <https://doi.org/10.1007/s10040-020-02267-y>

821 Li, Y., Wang, S., Peng, T., Zhao, G., & Dai, B. (2023). Hydrological characteristics and available  
822 water storage of typical karst soil in SW China under different soil–rock structures. *Geoderma*, 438,  
823 116633. <https://doi.org/10.1016/j.geoderma.2023.116633>

824 Goldscheider, Nico. (2015). Overview of Methods Applied in karst Hydrogeology. 10.1007/978-3-  
825 319-12850-4\_4.

826 Tapiador, F. J., Turk, F. J., Petersen, W., Hou, A. Y., García-Ortega, E., Machado, L. A. T., ...  
827 Huffman, G. J. (2012). Global precipitation measurement: Methods, datasets and  
828 applications. *Atmospheric Research*, 104–105, 70-97.  
829 <https://doi.org/10.1016/j.atmosres.2011.10.021>

830 Wang, S., Yan, Y., Zhao, Y., Fu, Z., & Chen, H. (2024). Co-evolution among soil thickness, epikarst  
831 weathering degree, and runoff characteristics on a subtropical karst hillslope. *Journal of Hydrology*,  
832 628\*, 130499. <https://doi.org/10.1016/j.jhydrol.2023.130499>

833 Fu, Z., Chen, H., Xu, Q., Jia, J., Wang, S., and Wang, K. (2016) Role of epikarst in near-surface  
834 hydrological processes in a soil mantled subtropical dolomite karst slope: implications of field  
835 rainfall simulation experiments. *Hydrol. Process.*, 30: 795–811. doi: 10.1002/hyp.10650.

836 Liu, X., Fu, Z., Zhang, W., Xiao, S., Chen, H., & Wang, K. (2023). Soluble carbon loss through  
837 multiple runoff components in the shallow subsurface of a karst hillslope: Impact of critical zone  
838 structure and land use. *CATENA*, 222\*, 106868. <https://doi.org/10.1016/j.catena.2022.106868>

839 Jasechko, S., Seybold, H., Perrone, D. *et al.* Rapid groundwater decline and some cases of recovery

840 in aquifers globally. *Nature* 625, 715–721 (2024). <https://doi.org/10.1038/s41586-023-06879-8>  
841 de Graaf, I.E.M., Gleeson, T., (Rens) van Beek, L.P.H. *et al.* Environmental flow limits to global  
842 groundwater pumping. *Nature* 574, 90–94 (2019). <https://doi.org/10.1038/s41586-019-1594-4>  
843 Liu, B., Chen, C., Lian, Y., Chen, J., & Chen, X. (2015). Long-term change of wet and dry climatic  
844 conditions in the southwest karst area of China. *Global and Planetary Change*, 127, 1-11.  
845 <https://doi.org/10.1016/j.gloplacha.2015.01.009>  
846 Hartmann, A., Goldscheider, N., Wagener, T., Lange, J., & Weiler, M. (2014). karst water resources  
847 in a changing world: Review of hydrological modeling approaches. *Reviews of Geophysics*, 52(3),  
848 218-242. <https://doi.org/10.1002/2013RG000443>  
849 D’Ettorre, U. S., Liso, I. S., & Parise, M. (2024). Desertification in karst areas: A review. *Earth-*  
850 *Science Reviews*, 253, 104786. <https://doi.org/10.1016/j.earscirev.2024.104786>  
851 Kang T, Lee S, Lee N, Jin Y. Baseflow Separation Using the Digital Filter Method: Review and  
852 Sensitivity Analysis. *Water*. 2022; 14(3):485. <https://doi.org/10.3390/w14030485>  
853 Rattayová, V., & Hlavčová, K. (2023). Base flow separation method in conditions of the karst  
854 catchment. *Pollack Periodica*, 18(2), 72-77.  
855 Helfer, F., Bernardi, F. K., Barros, C. A. P. de, Piccilli, D. G. A., Minella, J. P. G., Tassi, R., &  
856 Schlesner, A. A. (2024). Calibrated Eckhardt’s filter versus alternative baseflow separation methods:  
857 A silica-based approach in a Brazilian catchment. *Journal of Hydrology*, 644, 132073.  
858 <https://doi.org/10.1016/j.jhydrol.2024.132073>  
859 Zhou, X., Shen, C., Ni, G., & Hu, H. (2017). Digital filter-based baseflow separation method  
860 combined with recession curves. *Journal of Tsinghua University*, 57(03), 318-330.  
861 <https://doi.org/10.16511/j.cnki.qhdxxb.2017.26.016>  
862 Lebakula V , Sims K , Reith A ,et al.LandScan Global 30 Arcsecond Annual Global Gridded  
863 Population Datasets from 2000 to 2022. *Scientific Data*, 2025, 12(1).DOI:10.1038/s41597-025-  
864 04817-z.

865  
866  
867

### 868 **Author contributions**

869 Ze Yuan: Conceptualization, Methodology, Writing – original draft.  
870 Qiuwen Zhou: Formal analysis, Investigation, Writing – review & editing.  
871 Yuan Li: Data curation, Visualization, Software.  
872 Yuluan Zhao: Validation, Resources, Project administration.  
873 Shengtian Yang: Supervision, Funding acquisition, Writing – review & editing.

874  
875  
876

### 877 **Acknowledgments**

878 The authors thank all those who provided valuable assistance during the experimental  
879 process.